



Fluctuation Diagnostics in the 2D Hubbard model from the dual-fermion method

by

© **Behnam Arzhang**

A thesis submitted to the School of Graduate Studies
in partial fulfillment of the requirements for the
degree of Master of Physics.

Department of PHYSICS AND PHYSICAL OCEANOGRAPHY
Memorial University

November 2019

St. John's, Newfoundland and Labrador, Canada

Abstract

In this thesis, we use the Dual Fermion approximation (DF) to study the Hubbard model on the 2D square lattice by using two-particle quantities such as susceptibilities and full vertex functions.

In the first chapter we give an introduction to the strongly correlated systems including their definitions and features. Then, in the next chapter, to solve our model we present some numerical methods. The numerical methods that we used for our study are the dynamical mean-field theory (DMFT), the continuous-time auxiliary field impurity solver (CTAUX), Fluctuation diagnostics and Dual Fermion approximation (DF). The DF method provides high-resolution results for single-particle quantities such as the density of states (DOS) and Self Energy as well two particles spin susceptibility and vertex functions. With these results, we can present high-resolution results of the fluctuation diagnostics method with minimal computational expense. We examine the full Q -vector dependence of the extended self-energy at the Nodal and Antinodal k -points and provide interpretation for the claim that spin fluctuations are responsible for the observed metal-to-insulator behaviour.

Table of contents

Title page	i
Abstract	ii
Table of contents	iii
List of figures	v
List of symbols	vii
List of abbreviations	viii
1 Introduction	1
1.1 Strongly Correlated material	1
1.2 Fermi Liquid Theory	4
1.3 Hubbard Model	6
2 Theory and Method	9
2.1 Many Body Theory	9
2.1.1 Green's Function	10
2.1.2 Green's function of free fermions	12
2.2 Feynman Diagram	14

2.2.1	Self- Energy	15
2.3	Anderson Impurity Model	17
2.4	DMFT-impurity solver	19
2.5	Continuous Time Auxiliary Field (CT-AUX) algorithm	22
2.6	Susceptibility and Inversion of Bethe-Salpeter Equation	25
2.7	Dual Fermion method	30
2.8	Maximum Entropy Method (Maxent)	34
2.9	Fluctuation Diagnostics	36
2.10	Computational Methods	37
3	Results	38
3.1	Density of states	38
3.2	Dual Fermions (DF)	44
3.3	Fluctuation Diagnostics	49
3.3.1	Self-energy	50
3.3.2	$\Delta\Sigma$	54
4	Conclusion	59
	Bibliography	61

List of figures

1.1	Kmetko-Smith diagram	2
1.2	The spectral function of interacting and non-interacting systems	6
2.1	Non- interacting and interacting particles.	10
2.2	Feynman Diagram of Full Green's function, free Green's function and Coulomb interaction	14
2.3	Diagrammatic representation of Feynman diagrams introducing the ir- reducible self-energy $\Sigma^{(i)} = (k, \omega)$	15
2.4	Diagrammatic representation Feynman diagrams introducing the re- ducible self-energy Σ	16
2.5	Green's function as expansion of self-energy series.	16
2.6	Schematical representation of full Green's function.	17
2.7	The impurity Anderson model maps the physics of interacting electrons on a lattice onto a mean-field approximation.	17
2.8	Representation of Dynamical mean-field theory (DMFT).	20
2.9	The iterative self-consistent loop of Dynamical Mean-field theory. . . .	21
2.10	Particle-hole scattering.	26
2.11	Particle-Particle scattering.	26
2.12	Representation of Bubble and total part of susceptibility.	28
2.13	Color plot of Green's Function, output of Open- DF code.	33

2.14	Transformation of Green's function from Matsubara frequency to spectral function with real frequency.	36
3.1	Density vs μ based on single site DMFT results.	39
3.2	Density vs μ based on Dual Fermion approach.	40
3.3	Spectral function $A(\omega)$, output of Maxent from DMFT results.	42
3.4	Spectral function, output of Maxent from Open- DF results.	43
3.5	Imaginary part of the self energy as a function of Matsubara index for the DF Nodal (N) and Anti-nodal (AN).	44
3.6	Analytic continuation result for the spectral function.	45
3.7	$\Delta\Sigma$ at the nodal ($\Delta\Sigma_N$) and antinodal ($\Delta\Sigma_{AN}$) momenta as a function of density.	46
3.8	Curve fitting plots	47
3.9	Density dependence of the anti-ferromagnetic correlation length.	48
3.10	the effect of different cut off frequency on the self-energy.	51
3.11	Imaginary part of the self energy for the antinodal and nodal vs momenta.	52
3.12	Decomposition of imaginary part of the single particle self energy into $+\Omega$ and $-\Omega$	53
3.13	Decomposition of imaginary part of the single particle self energy from Fig. 3.5 into $+\Omega$ and $-\Omega$ contributions and the $\Omega = 0$	54
3.14	Decomposition of the imaginary part of the self-energy into its ω_0 and ω_1	55
3.15	Color Plots: $\Delta\Sigma^{(\Omega)}(q_x, q_y)$ for nodal and anti- nodal momenta.	57
3.16	Cuts of $\Delta\Sigma^{(\Omega)}(q_x, q_y)$ along the path from $(0, \pi) \rightarrow (2\pi, \pi)$, $(\pi, 0) \rightarrow (\pi, 2\pi)$, and $(0, 0) \rightarrow (2\pi, 2\pi)$	58

List of symbols

Σ	Self-energy
χ	susceptibility
ξ	Correlation length
G	Green's function
F	Vertex function

List of abbreviations

DMFT	Dynamical Mean Field Theory
DF	Dual Fermions
DOS	Density of State
N	Nodal points
AN	Anti- Nodal points

Chapter 1

Introduction

1.1 Strongly Correlated material

Modern solid-state physics tries to explain the physical properties of different materials such as simple metals, semiconductors and insulators. But some materials in which their d and f electron shells are not fully occupied and electrons occupy narrow orbitals show complicated properties [1]. For example, transition metals V, Fe, Ni, and their oxides, or rare- earth metals such as Ce belong to this group. This situation, where there is an open d or f electron shell, increases the effect of the Coulomb interaction between the electrons. These materials with strong electron-electron interaction are strongly correlated systems [2]. As mentioned before these materials show complicated and interesting features: phase transitions between magnetic order and superconductivity, appearance and disappearance of local magnetic moments, transport property anomalies [3]. As example, some strongly correlated systems can be listed as below [2]:

- Cuprate superconductors,
- Heavy-electron compounds,
- Fractional quantum Hall systems,
- Quantum dots,
- Cold atomic gases,

A huge number of strongly correlated materials have atoms which are not fully occupied in d or f orbitals. Heavy-electron materials are an excellent example of this group, the component of the electron fluid, which is extremely localized in f orbitals, create magnetic moments. The driving force for the strongly correlated electrons systems is provided by the interplay of the conduction electrons with localized magnetic moments [2].

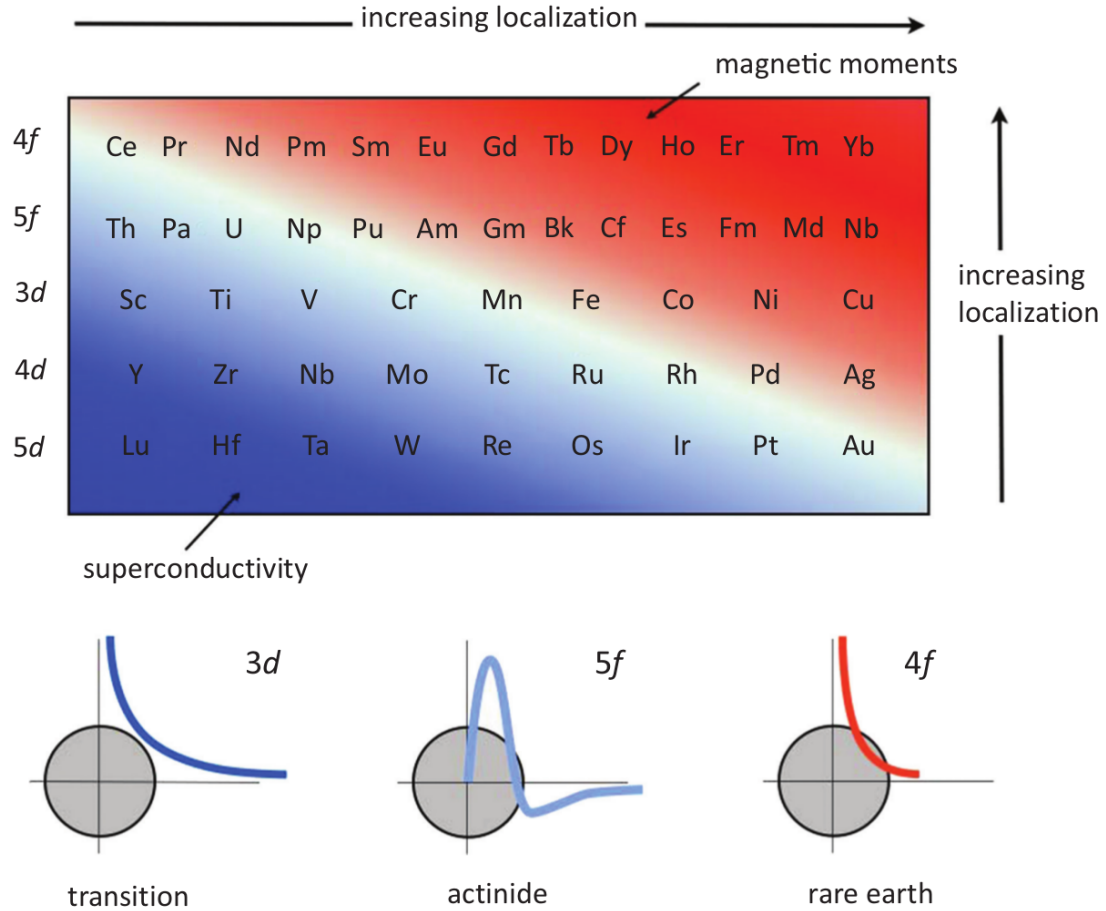


Figure 1.1: Kmetko-Smith diagram, displaying the behaviour of elements based on increasing electron localization in d and f electron orbitals [2].

The behaviour of strongly correlated electrons can be predicted based on the specific pattern in the periodic table. The most strongly interacting electrons are those with partially filled orbitals and are localized around the nucleus. In the narrow electron bands systems, orbitals of neighbouring atoms have weak overlap, while electrons in the well-localized orbitals show strong interaction[2].

The position of strongly correlated elements in periodic table is shown in the Figure 1.1 which is known as a *Kmetko-Smith* diagram. For elements in the right side of the diagram from bottom to up the localization will increase. The d-orbitals of metals which are in the bottom left-hand side of the diagram are conventional superconductors. By contrast, electrons in the actinide ions or rare-earth in the metals in the top right-hand side of this diagram are well localized, which leads to forming magnets or antiferromagnets [2].

Finding a complete theoretical explanation for strongly correlated systems is one of the biggest challenges for scientists, because of the fact that they cannot treat these materials as an ensemble of free particles. The new properties that these materials reveal are because of the existence of electron-electron interaction [4]. This complexity needs new theories that are entirely different from old approaches like *ab initio* methods and band theory, which are unable to explain these new features [1]. For instance, in high T_c cuprates, band theory in hole-doped region predicts that it is metal while in fact it is Mott-insulator, and Fermi liquid theory is unable to explain its behaviour in the strange metal (nFL) and pseudogap region [5, 6]

To get a comprehensive understanding of strongly correlated materials, different theoretical techniques have been developed, each of these methods has its computational advantages. Some of these numerical techniques that researchers use to find the solution of strongly correlated materials are Dynamical Mean Field Theory (DMFT), Quantum Monte Carlo (QMC) and Exact Diagonalization (ED) [1, 7], auxiliary-field quantum Monte Carlo (AFQMC) [8], density matrix renormalization group theory (DMRG) [9] the dynamical cluster approximation (DCA) [10] and the dual fermion method (DF) [11].

In this thesis, we will describe the 2D Hubbard model. Then in chapter 2 we will discuss some theoretical and numerical methods which we used in this work and tried to solve and simulate the 2D Hubbard model, such as dynamical mean field theory (DMFT), the continuous time auxiliary field algorithm (CTAUX), and the Maximum Entropy Method (Maxent) for numeric analytic continuation, Dual Fermion method (DF) and Fluctuation Diagnostics.

The Dual Fermion method is used to compute corrections for single-site DMFT simulations. The Dual Fermion method has this feature that helps us to access arbitrary momenta throughout the Brillouin zone, in contrast to the limitation to a few

cluster momenta that characterize cluster methods like DCA. Also, we used Bethe-Salpeter equation to find full vertex function F for different channels of spin-spin, particle-particle, and particle-hole (sp, pp, ph) and by replacing full vertex function F in the self-energy, we can find the effect of different scattering channel on self-energy.

In chapter 3, we will present our result obtained from DMFT and Dual Fermion methods. We will show that corrections that DF applies on the DMFT results will increase the accuracy of our procedure in a way that we can see Metal-Insulator transition happens in smaller U for Dual fermion spectral function in comparison with DMFT results. Then we discuss the transition from Fermi liquid state to non-Fermi liquid state based on self-energy result obtained from DMFT and Dual Fermion methods. The high momentum resolution self-energy and $\Delta\Sigma$ will be discussed. Finally, in chapter 4, we will summarize our results and our method.

1.2 Fermi Liquid Theory

Our basic knowledge about simple metals is based on the free electron theory. In the free electron model, non-interacting electrons move freely in a positive charge background [12]. Although this model is simple, it can explain many fundamental properties of metals. For example, Drude suggested the Ohm expression based on this model [13]. Later Sommerfeld introduced a new theory called the Fermi-gas model, where there are no interactions between electrons. In this model, electrons are considered as quantum particles, and Schrodinger equation is used to explain their behaviour. Also, electrons follow Fermi-Dirac statistic. Electrons fill up the available states, according to the Pauli-exclusion principle, up to the Fermi surface [12, 14].

However, in real metals, there are some interactions among particles. Lev Landau in the 1950s addressed this problem by introducing the quasiparticles at low temperatures and low excitation energies in an interacting fermion system. In this model, the assumption is that the behaviour of quasiparticles lying on the Fermi surface is influenced by the interaction, Landau then introduced the Landau parameters to describe the effective interaction between quasiparticles. [15, 16].

Landau in this theory determined the expressions for the effective mass, specific heat, magnetic susceptibility by using the concept of Landau parameters [16, 17]:

$$\frac{m^*}{m} = 1 + \frac{F_1^s}{3} \quad (1.1)$$

where m is the electron mass, m^* is the effective mass of quasiparticles and F_1^s Landau parameter. Experiments cannot measure the effective mass directly, but it shows itself in other measurable quantities such as the specific heat capacity C_ν or susceptibility χ :

$$C_\nu = \frac{m^* p F}{3\hbar} k_B^2 T \quad (1.2)$$

$$\chi = \frac{m^* p F}{\pi^2 \hbar^3} \frac{\beta^2}{1 + F_0^a} \quad (1.3)$$

Fermi-liquid theory is the central tool to investigate the simple metals. It also holds even in extreme cases such as some heavy-Fermion systems and high- T_c superconductors, where strong correlations are present.

A practical way to find out that the system is in the Fermi liquid region or it is in non-Fermi liquid region is to find its spectral function. The spectral function $A(k, \omega)$ reveals the energy distribution of a system during the process of adding or withdrawing a particle with momentum k . As it is shown in Fig. 1.2 (a) for a system of non-interacting particles, the spectral function $A_0(k, \omega)$ is a δ function with a peak at the energy ϵ_k since electrons are eigenstates of the system [18, 19]. While, in the interacting system, an electron may take part in different eigenstates of the system; therefore, the spectral function is spread out in energy. For momenta near k_F it is possible that the electron might be seen in the quasiparticle eigenstate with momentum k . So the spectral function of the electron at $T = 0$ in a Fermi liquid would have a sharp peak at the new quasiparticle energy.

However, there are other materials which show new properties. These materials are known as non-Fermi liquid. Some examples of these systems are Heavy Fermions [20] and system of interacting fermions in one dimension which is called the Luttinger liquid [21]. Non-Fermi-liquid behaviour usually can be seen experimentally near a magnetically ordered phase in the phase diagram, which shows the non-Fermi-liquid state in the system may be related to a magnetic instability that appears at $T = 0$ [20].

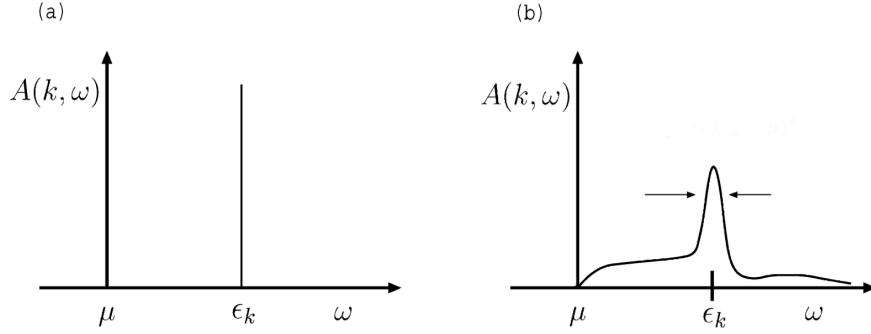


Figure 1.2: The spectral function interacting and non-interacting system: (a) In a non-interacting system, electrons are eigenstates and so the probability is a δ function centred on the electron energy, ϵ_k . (b) In the Fermi liquid system, the probability is spread out with a peak at the new quasiparticle energy. Taken from Ref. [19] with permission.

1.3 Hubbard Model

The Hubbard model was introduced in 1963 in two different papers, first by Gutzwiller [22], and then Hubbard [23]. They tried to explain the effect of correlations for d-electrons in transition metals in a simple way[24]. Different models have been proposed to study the many-body aspects of the electronic properties of condensed matter, but the Hubbard model is maybe the simplest model. This model tries to simplify the physics of matter by including only an effective local interaction. It means complexities of atomic physics and the corresponding multi-band description of condensed matter have been neglected[25]. As mentioned one of the main motivations to study the Hubbard model is that, not only is it the simplest generalization beyond the band theory description of solids, but also it seems it can explain the main physical features of many systems. The Hubbard model has been used to describe[26]:

- the electronic properties of solids with narrow bands,
- band magnetism in iron, cobalt, nickel,
- the Mott metal-insulator transition,
- electronic properties of *high* – T_c cuprates in the normal state.

The Hamiltonian of the Hubbard model is:

$$H = -t \sum_{\langle i,i' \rangle, \sigma} (c_{i,\sigma}^\dagger c_{i',\sigma} + c_{i',\sigma}^\dagger c_{i,\sigma}) + U \sum_{i=1}^N n_{i\uparrow} n_{i\downarrow}. \quad (1.4)$$

In this formula i, i' label the sites of a D-dimensional lattice, $c_{i,\sigma}^\dagger (c_{i,\sigma})$ are creation(annihilation) operators which create (annihilate) an electron of spin $\sigma(\uparrow, \downarrow)$ on a site i , $n_{i\sigma} = c_{i,\sigma}^\dagger c_{i,\sigma}$ is an electron number operator which counts the number of electrons with spin σ at site i . The first term in the Hubbard model Hamiltonian is chemical bonding and is known as "hopping" which represents a single particle interaction and hops an electron from one atom to the nearest neighbour atom with hopping matrix element t . The second term is related to two particle interaction, it explains the Coulomb repulsion between two electrons. The long-range contribution is neglected and only the interaction when both the electrons are on the same atom is retained, generating an energy of U when the atom is doubly occupied [25]. In Eq (1.4) when $U > 0$ it represents repulsive Coulomb interaction, and $U < 0$ corresponds to an effective attractive interaction between the electrons [24].

It is expected that Eq (1.4) describes the main features of the materials, namely itinerant magnetism and metal-insulator (Mott) transition. When $U = 0$, H reduces to a non-interacting system of moving electrons, and for $t = 0$ (atomic limit) the electrons are fully localized, and the system is insulator. In addition, for finite t and $U = \infty$, the corresponding system is an antiferromagnetic insulator. [24].

Many efforts have been devoted to finding the solution of the Hubbard model. 3. However, there is not an exact general solution that we can apply to all problems, and existing solutions are mainly restricted to the one-dimensional case, in which there is no metal-insulator transition at any $T \neq 0$. Even at $T = 0$ the exact solution doesn't show metal-insulator transition for any $U > 0$. It is thought that the interplay between magnetic behaviour and the Mott transition near half-filling in the superconductors is crucial, since not only most of the new ceramic superconductors are good Mott insulators, but also they can show strong antiferromagnetic correlations, and the antiferromagnetic phase is close to the superconducting phase. It is shown that superconductivity can exist for $U < 0$, but for repulsive interaction it is not clear whether this is still true or not [24].

Cuprate is quasi-two-dimensional materials and electrons which move within weakly

coupled layers determine their superconducting properties. This material can be doped (amount of free charge carriers) by electrons or holes, and their superconductivity properties would change based on this doping level. The undoped compounds are Mott insulators with long-range antiferromagnetic order. Hubbard model is considered to describe the electronic properties of these two-dimensional materials.

Chapter 2

Theory and Method

2.1 Many Body Theory

Many-body problems refer to systems with many particles (many electrons, many atoms, many molecules, etc.), where there are interactions among them. Imagine that there is no interaction between particles. In that case, each particle is like an independent body, and there is no relation between all bodies in the system such that we can study the behaviour of each body independently. In fact, when there is no interaction, the problem of one many-body system changes to many one-body systems. Consequently, interactions are the basic part of many-body problems [27].

The importance of many-body problems raises from the fact that all of the real physical systems include particles. For instance, the interaction between nucleons in a nucleus is governed by the nuclear force, electrons in an atom or metal interact by Coulomb forces, and atoms are bonded together by electrostatic attraction.

The many-body problem is one of the most challenging dilemmas in physics since there is complex motion of particles in an interacting system. In Fig.2.1 the behaviour non-interacting and interacting particles can be seen. Non-interacting particles have simple behaviour while interacting particles show complicated behaviour referred as emergent phenomena [28].

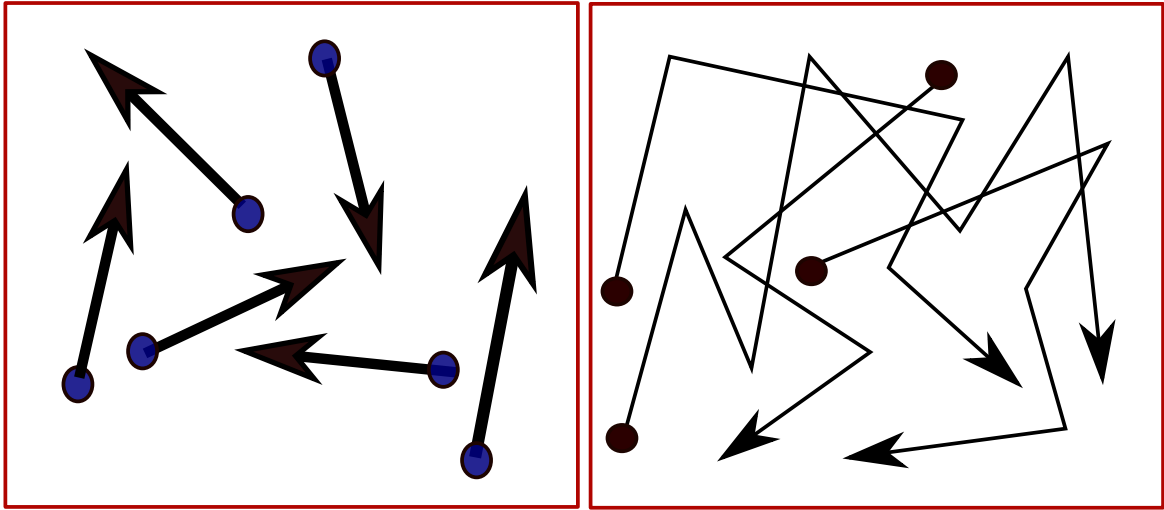


Figure 2.1: Non- interacting and interacting particles.

2.1.1 Green's Function

The Green's function method has different applications in several fields of Physics, from classical differential equations to quantum many-body problems. For example, in the context of quantum mechanics, Green's functions are correlation functions, from which it is possible to extract some information such as the density of states, relaxation times and response functions from the system. Green's functions theory is a useful mathematical tool to deal with linear differential equations. These functions were named after physicist and mathematician George Green (1793-1841). The Green's functions were used as auxiliary functions for solving boundary-value problems. Moreover, a Green's function is a solution of a linear differential equation with a Dirac delta inhomogeneous source (sometimes referred as a delta or unit pulse) with homogeneous boundary conditions [29]. Usually, the problems that we are dealing with are many body systems of quantum particles interacting with each other or with quantized versions of classical waves. 4. To obtain physically relevant information about the properties of these interacting many-particle systems, the definition of the Green's functions should include all general Feynman diagrams[30].

As mentioned above, Green's functions are the elementary response functions of a many-body system to an external force. The one- particle Green's function can be defined as[2]:

$$G_{\lambda\lambda'}(t-t') = -i\langle\phi|T\psi_\lambda(t)\psi_{\lambda'}^\dagger(t')|\phi\rangle \quad (2.1)$$

In this equation $|\phi\rangle$ is the many-body ground state and $\psi_\lambda(t)(\psi_{\lambda'}^\dagger(t'))$ are annihilation (creation) operators, λ denotes the momentum and spin of the particle $\lambda \equiv P\sigma$, and

$$T\psi_\lambda(t)\psi_{\lambda'}^\dagger(t') = \begin{cases} \psi_\lambda(t)\psi_{\lambda'}^\dagger(t') & (t > t') \\ \pm\psi_{\lambda'}^\dagger(t')\psi_\lambda(t) & (t < t') \end{cases} \quad (2.2)$$

represents the time-ordering for fermions and bosons ($-$ is used for Fermions and $+$ for Bosons). In fact, the time ordering operator takes products of operators, that each operator belongs to a specific time, and modifies the order of operators in a way that every operator has only later operators to its left and earlier operators to its right. Then

$$G_{K\sigma,K',\sigma'}(t-t') = \delta_{\sigma\sigma'}\delta_{KK'}G(K,t-t') \quad (2.3)$$

is diagonal in K and K' (in the continuum limit $\delta_{KK'}$ is $(2\pi)^D\delta^{(D)}(K-K')$). Now we can write:

$$G(K,t-t') = -i\langle\phi|T\psi_{K\sigma}(t)\psi_{K\sigma'}^\dagger(t')|\phi\rangle \quad (2.4)$$

and in the space coordinate the Green's functions can be written as:

$$G(X-X',t-t') = -i\langle\phi|T\psi_\sigma(X,t)\psi_{\sigma'}^\dagger(X',t')|\phi\rangle. \quad (2.5)$$

By replacing $\psi(X,t)$ with $\int_K \psi_{K\sigma} e^{i(K.X)}$, it can be seen that the coordinate-space Green's function is equivalent to the Fourier transform of the momentum-space Green's function:

$$G(X-X',t) = \int_{K,K'} e^{i(K.X-K'.X')} -i\langle\phi|T\psi_{K\sigma}(t)\psi_{K'\sigma}^\dagger(0)|\phi\rangle \quad (2.6)$$

where

$$-i\langle\phi|T\psi_{K\sigma}(t)\psi_{K'\sigma}^\dagger(0)|\phi\rangle = \delta_{KK'}G(K, t-t'), \quad (2.7)$$

such that Eq (2.6) reduces to:

$$\int \frac{(d^3k)}{(2\pi)^3} G(K, t) e^{iK \cdot (X-X')} \quad (2.8)$$

The Fourier transform of this equation in the time domain is:

$$G(K, t) = \int_{-\infty}^{\infty} \frac{d\omega}{2\pi} G(K, \omega) e^{-i\omega t}. \quad (2.9)$$

In this equation ω is frequency and $G(K, \omega)$ is the frequency dependent Green's function:

$$G(K, \omega) = \int_{-\infty}^{\infty} dt G(K, t) e^{-i\omega t}. \quad (2.10)$$

Now we are in a position to relate the Green's function in coordinate space to its propagator:

$$-i\langle\phi|T\psi_{\sigma}(X, t)\psi_{\sigma'}^\dagger(X', t')|\phi\rangle = \int \frac{d^3k d\omega}{(2\pi)^4} G(K, \omega) e^{i[K \cdot (X-X') - \omega(t-t')]} \quad (2.11)$$

2.1.2 Green's function of free fermions

Now we can calculate the Green's function of a degenerate Fermi liquid of non-interacting fermions in its ground state. We use an interacting Hamiltonian which is in the Heisenberg representation:

$$H = \hat{H}_0 - \mu N = \sum_{\sigma} \epsilon_K c_{K\sigma}^\dagger c_{K\sigma}. \quad (2.12)$$

In this equation $\epsilon_K = \frac{\hbar^2 k^2}{2m} - \mu$ and $c_{K\sigma} (c_{K\sigma}^\dagger)$ is the creation (annihilation) operator of fermions in momentum space. The wave function of the ground state for a fluid of fermions is:

$$|\phi\rangle = \prod_{\sigma|K| < k_f} c_{K\sigma}^\dagger |0\rangle. \quad (2.13)$$

In the Heisenberg picture, time propagation of the system $c_{K\sigma}^\dagger(t) = e^{i\epsilon_K t} c_{K\sigma}^\dagger$, $c_{K\sigma}(t) = e^{-i\epsilon_K t} c_{K\sigma}$. To go forward in the time domain, we are allowed to add a fermion above the Fermi energy, so:

$$\begin{aligned} \langle\phi|c_{K\sigma}(t)c_{K'\sigma'}^\dagger(t)|\phi\rangle &= \delta_{\sigma\sigma'}\delta_{KK'}e^{-i\epsilon_K(t-t')}\langle\phi|c_{K\sigma}c_{K'\sigma'}^\dagger|\phi\rangle \\ &= \delta_{\sigma\sigma'}\delta_{KK'}(1 - n_K)e^{-i\epsilon_K(t-t')} \end{aligned} \quad (2.14)$$

In the last equation $n_K = \theta(|k_F| - |K|)$ is Heaviside step distribution. For backward time propagation we need to annihilate a fermion and create a hole beneath the Fermi energy, so:

$$\langle\phi|c_{K'\sigma'}^\dagger(t)c_{K\sigma}(t)|\phi\rangle = \delta_{\sigma\sigma'}\delta_{KK'}n_Ke^{-i\epsilon_K(t-t')} \quad (2.15)$$

then by using Eq. 2.11 we can find

$$G(K, t) = -i[(1 - n_K)\theta(t) - n_K\theta(-t)]e^{-i\epsilon_K t} \quad (2.16)$$

This equation can be expressed for two different situation:

$$G(K, t) = \begin{cases} -i\theta_{|K|-|K_F|}e^{-i\epsilon_K t} & (t > 0) & \text{particles} \\ i\theta_{|K_F|-|K|}e^{-i\epsilon_K t} & (t < 0) & \text{holes : particles moving backwards in time} \end{cases} \quad (2.17)$$

Now we are in a place that we can find the Fourier transform of the free fermion's Green's function:

$$\begin{aligned} G(K, \omega) &= -i \int_{-\infty}^{\infty} dt e^{i(\omega - \epsilon_K)t} [\theta_{k-k_F}\theta(t) - \theta_{k_F-k}\theta(-t)] e^{-|t|\delta} \\ &= -i \left[\frac{\theta_{k-k_F}}{\delta - i(\omega - \epsilon_K)} - \frac{\theta_{k_F-k}}{\delta + i(\omega - \epsilon_K)} \right] \end{aligned} \quad (2.18)$$

In this equation $e^{-|t|\delta}$ is called *convergence factor*. We introduced this term to make the integrals converge, we use the $\lim \delta \rightarrow 0^+$. Then the free fermion propagator can be written as

$$G(K, \omega) = \frac{1}{\omega - \epsilon_K + i\delta_K}, \quad (2.19)$$

where $\delta_K = \delta(\text{sgn}(k - k_F))$.

2.2 Feynman Diagram

Feynman diagrams are a powerful tool for quantum theory calculations. Richard P. Feynman introduced this method to explain quantum interactions [31, 32, 33]. Feynman diagrams usually include all information about the diagrams and the process of constructing the mathematical expression of the diagrams. There are some specific rules for this method known as "Feynman rules". The solid straight lines introduce the fermions, wavy lines represent Bosons, and dots or vertices are for the coupling [32, 33].

By Wick's theorem¹, we can evaluate the exact Green's functions as a perturbation expansion involving expressions of free Green's functions G_0 and the perturbation potential V . That representation is equivalent to the Feynman diagram approach. The Feynman diagrams are a demonstrative way to solve the many-particle problems and the perturbation expansion of the Green's functions [34, 35, 36].

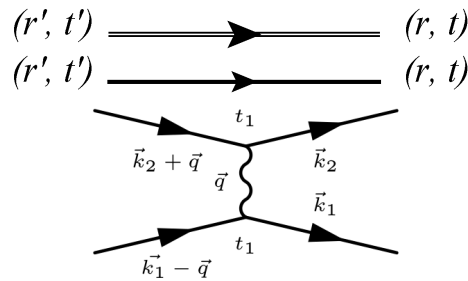


Figure 2.2: Feynman Diagram of Full Green's function, free Green's function and Coulomb interaction, respectively.

¹Wick's theorem is used to reduce a product of creation and annihilation operators as a sum of normally ordered terms.

Shown in Fig. 2.2, the Green's function can be represented as the creation of a particle at (r', t') then it will propagate to the point (r, t) where the particle is annihilated. In the Feynman diagram representation, the full Green's function is shown by a double line joining these two points, and the free Green's function is described by a single line. Also, the Coulomb potential is drawn by a wavy line, at the vertex, the momentum and energy are conserved [37, 38].

2.2.1 Self- Energy

The feedback of the interacting environment on a propagating particle can be understood by the concept of self-energy [2]. The self-energy $\Sigma(\vec{k}, \omega)$ can be found as the sum of all diagrams that cannot be broken into two by breaking a single internal fermion line (The left arm and right arm are electron lines in a diagram which are called external, and all other electron lines are called internal). It should be mentioned that in the self-energy diagrams there must be a momentum \vec{k} and energy ω coming in and going out. But the Green function lines that carry this energy and momentum to the vertices are not included [37, 27]. Some examples of irreducible diagram is shown in Fig. 2.3 [27]. It is clear that by cutting a Fermion line, we can not find a new diagram.

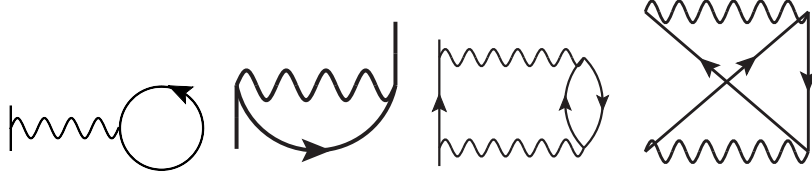


Figure 2.3: Diagrammatic representation of Feynman diagrams introducing the irreducible self-energy $\Sigma^{(i)} = (k, \omega)$.

If a diagram is not irreducible or on the other hand it can be separated, it is called reducible and it's a part of the Green's function. some examples can be seen in Fig. 2.4 [27]:

Now we are in a position that we can define a mathematical expression for the self-energy diagram by using the Feynman rules, as we know the self-energy is the sum of all irreducible Feynman diagrams. It is the same as that of the irreducible diagram it was constructed from except the external lines of $G_0(k, \omega)$ [39].

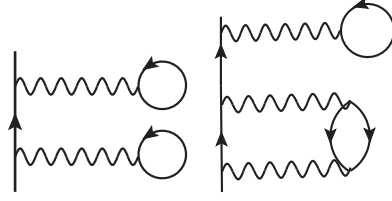


Figure 2.4: Diagrammatic representation Feynman diagrams introducing the reducible self-energy Σ .

$$\Sigma(k) = \sum_i \Sigma^{(i)}(k) \quad (2.20)$$

Now we can show that the particle propagator can be extended as self-energy series in Fig. 2.5 [2, 40]:

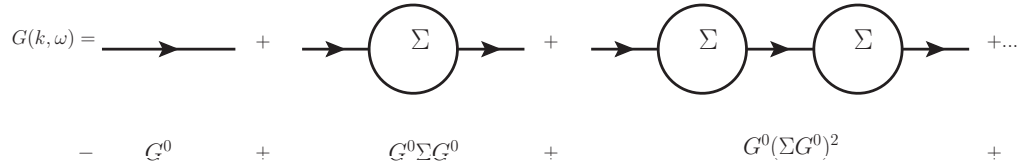


Figure 2.5: Green's function as expansion of self-energy series.

This graphical expansion can be written in mathematical language as:


$$G(k, \omega) = \frac{G_0(k, \omega)}{1 - \Sigma(k, \omega)G_0(k, \omega)} = \frac{1}{(G_0(k, \omega))^{-1} - \Sigma(k, \omega)} \quad (2.21)$$

then Eq. 2.21 can be written as:

$$G(k, \omega) = \frac{1}{\omega - \epsilon_k - \Sigma(k, \omega) + i\delta}. \quad (2.22)$$

This equation is known as the Dyson equation. Now we can see that the full Green's function is determined by the Dyson equation [2, 40].

The equation we represented in Fig. 2.6 is called Dyson equation. Physically, the self-energy which is a complex function ($Re + iIm$) represents the cloud of particle-hole excitations which follow the propagating electron, "dressing" it into a quasiparticle [41, 34, 2].



$$G(k, \omega) = G^0(k, \omega) + G^0(k, \omega) \Sigma(k, \omega) G(k, \omega)$$

Figure 2.6: Schematic representation of full Green's function. The full Green's function can be obtained by using the Dyson equation.

2.3 Anderson Impurity Model

The Anderson impurity model was originally introduced by Anderson in the 1961 to describe the behaviour of magnetic impurities (Fe, Mn, Cr) diluted into non-magnetic metals [42]. In those systems, an anomalous minimum in the electrical resistivity at low temperatures was seen, for which the interaction of impurities and the conduction electrons seems to have caused this phenomenon [43]. The impurity Anderson model maps a lattice site of interacting electrons onto a mean-field approximation. In the lattice problem, the electrons repulse each other via the on-site Coulomb repulsion U , and they can move in the lattice sites by the hopping parameter t [42]. In Fig. 2.7 schematical representation of Anderson impurity model has been shown.

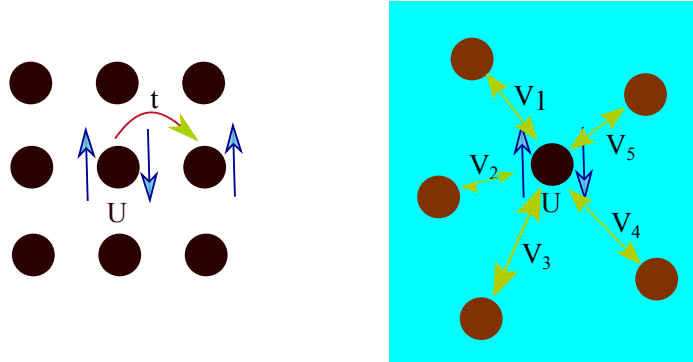


Figure 2.7: The impurity Anderson model maps the physics of interacting electrons on a lattice onto a mean-field approximation. In the lattice problem, the electrons repulse each other via the on-site Coulomb repulsion U , and they can move in the lattice sites based on the hopping parameter t .

The Anderson model is an important ingredient of the dynamical mean field theory for correlated lattice models, which will be further discussed. The Hamiltonian of the

Single Impurity Anderson Model (SIAM) includes three different parts [44]:

$$H_A = H_a + H_b + H_h \quad (2.23)$$

where the second term

$$H_b = \sum_k \epsilon_k c_{k\sigma}^\dagger c_{k\sigma} \quad (2.24)$$

Here ϵ_k is the energy of electron in the conduction band and it is measured from the Fermi energy, $c_{k\sigma}^\dagger$ and $c_{k\sigma}$ are creation and annihilation operators and σ describes spin. The first term is

$$H_a = \epsilon_d n_d + U n_{d\uparrow} n_{d\downarrow}, \quad (2.25)$$

describes the interacting electron level, where ϵ_d is the energy of electrons in the localized impurity state, the total occupancy of the impurity level is $n_d = n_{d\uparrow} + n_{d\downarrow}$, and $U > 0$ represents the Coulomb repulsion between a pair of localized electrons. Finally, the last term is

$$H_h = \sum_k \frac{t_k}{\sqrt{N_0}} (c_{k\sigma}^\dagger d_\sigma + H.c.). \quad (2.26)$$

Where the number of unit cells in the host is given by N_0 , t_k is the hybridization matrix elements, and $H.c$ introduces the hermitian conjugate.

In Eq. 2.26 we replace $V_k = \frac{t_k}{\sqrt{N_0}}$, and introduce the hybridization function $\Delta(\omega)$ which is the coupling of the impurity to the band [45]:

$$\Delta(\omega) = \sum_{k\sigma} \frac{|V_k|^2}{\omega - \tilde{\epsilon}_k} \quad (2.27)$$

The local free Green's function can be express as:

$$\mathcal{G}_0^{-1}(\omega) \equiv \omega + \mu - \Delta(\omega) \quad (2.28)$$

The interacting Anderson Green's function will be:

$$G_A = \frac{1}{\omega + \mu - \Delta(\omega) - \Sigma(\omega)} \quad (2.29)$$

In the Eq. 2.29 the $\Sigma(\omega)$ is self-energy.

2.4 DMFT-impurity solver

The dynamical mean-field theory was introduced by Metzner and Vollhardt in 1989 [46]. It has become one of the most important tools for the study of strongly correlated electrons systems. The mean-field theory replaces a lattice problem with many degrees of freedom by a single-site effective problem with fewer degrees of freedom [47]. It has been shown that the Hubbard model could be mapped exactly to the Anderson impurity model in the limit of infinite coordination number ² [46]. In the interacting lattice, one site is chosen, and all other sites are mapped into a bath. Therefore, the lattice model is mapped to an "impurity" model that includes one single interacting site ("impurity"), which is coupled to the non-interacting bath [47].

Electrons in a crystals lattices of finite dimension can leave a site by hopping to a neighbouring site. It also can return to the original site by just hopping backward, or in a complicated way, by hopping around a loop to get to the original site. The easiest problem to solve is the Bethe lattice ³ since there are no loop paths, it means if an electron hops off of a site, it can only return to the original site by reversing its path. In the DMFT when the number of neighbours N increases, the probability of returning the electron to the original site by another paths decreases. Therefore, when $N = \infty$ it becomes impossible, by increasing N the mean field theory becomes an exact theory [48]. Dynamical mean-field theory (DMFT) maps the lattice of atoms and electrons to a single impurity atom and a bath of electrons this process is shown in Fig.2.8. Over time a lattice site can be unoccupied, occupied or doubly occupied by electrons. Impurity and bath are coupled together.

The lattice model we study is the Hubbard model, and it will be mapped to an Anderson impurity model (AIM) and we will use the DMFT self-consistency loop

²The number of ions, molecules or atoms which surround the central ion, molecule or atom is called Coordination number.

³A Bethe lattice is an infinite connected node that each node is connected to z coordination number.

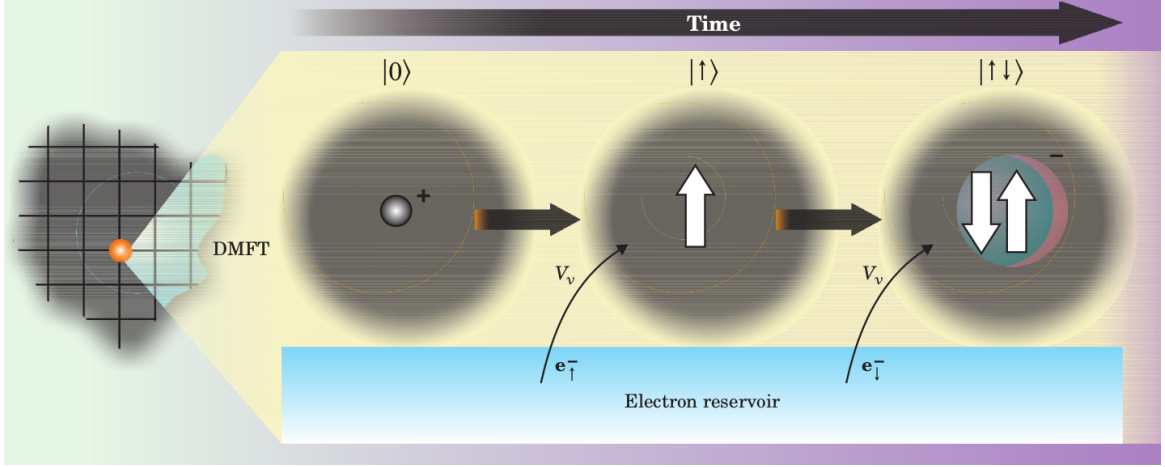


Figure 2.8: Dynamical mean-field theory (DMFT) maps the full lattice of atoms and electrons with a single impurity atom in a bath of electrons. Over time a lattice site can be unoccupied, occupied or doubly occupied by electrons. These dynamical processes, which results in time-resolved electron- electron interactions are taken into account in DMFT. Taken from ref [1] with permission.

which is shown in Fig.2.9 [47]. We can write the self-consistency loop as Fig.2.9:

In the first step, we start from the solution of the Anderson Impurity Model (AIM), the self-energy $\Sigma(\omega)$. Then, we assume that the lattice self-energy is local, it means that lattice self-energy is k -independent and can be set equal to the self-energy of the impurity (DMFT approximation), $\Sigma_{Lat}(K, \omega) \approx \Sigma(\omega)$ [47]. Therefore, the lattice Green's function can be express as:

$$G_{Lat}(\omega) \equiv G_{Lat}(X = 0, \omega) = \sum_K e^{iXK} G_{Lat}(K, \omega) = \int d\epsilon \frac{\rho(\epsilon)}{\omega + \mu - \epsilon - \Sigma(\omega)}. \quad (2.30)$$

In Eq.2.30, $\rho(\epsilon) = \sum_K \delta(\epsilon - \epsilon_K)$ is the density states of the band. The self-consistency condition forces the impurity and the lattice Green's functions to be equal $G_{Lat} = G_A$, which is equivalent to the mapping of the lattice to the impurity model. Then we can write the self-consistency equation as:

$$G_{Lat}^{-1}(\omega) = \mathcal{G}_0^{-1}(\omega) - \Sigma(\omega). \quad (2.31)$$

The free Green's function of the impurity model $\mathcal{G}_0(\omega)$ includes all the information

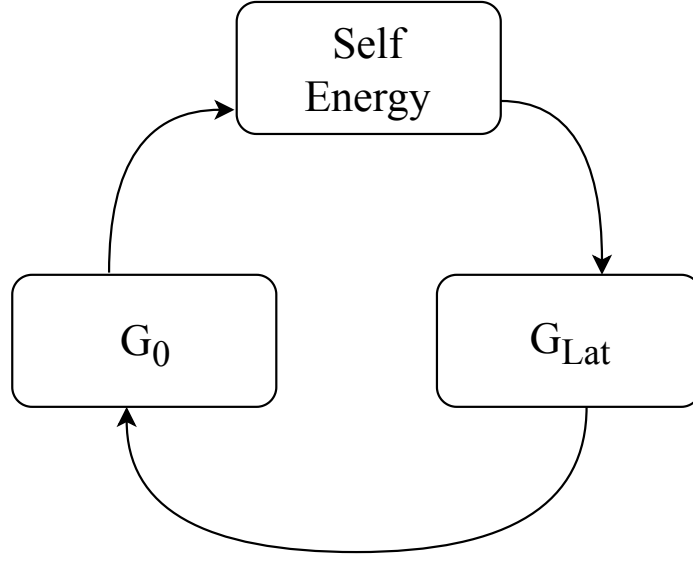


Figure 2.9: The iterative self-consistent loop of Dynamical Mean-field theory. By repeated iterations, a self-consistent solution will be found.

of the bath of the single site. By using Eq. 2.31, the bath of the Anderson impurity model ($\mathcal{G}_0(\omega)$), can be computed with (G_{Lat}) and (Σ). Finally, $\Sigma(\omega)$ will be calculated in the last step, these steps and loop can be seen in Fig. 2.9. Thus the loop is closed, and by repeated iterations, a self-consistent solution will be found. The steps that we mentioned above can be listed as below:

- Start with arbitrary self-energy $\Sigma(\omega)$.
- Find the lattice Green's function from Eq. 2.30.
- Find the dynamical mean-field ($\mathcal{G}_0(\omega)$) from Eq. 2.31.
- Use the dynamical mean-field impurity solver to find the new Green's function.
- By replacing new Green's function in Eq. 2.31 the self-energy can be found.
- These steps will continue until the self-energy converge.

2.5 Continuous Time Auxiliary Field (CT-AUX) algorithm

The central numerical effort in solving the dynamical mean field problems is solving the quantum impurity problem, by finding a self-energy for a specific Green's function. In this section we introduce the Continuous Time Auxiliary Field (CT-AUX) algorithm that we used as the DMFT impurity solver. Continuous-time quantum Monte Carlo (CT-QMC) is a method for solving the Anderson impurity model at finite temperature [49, 50, 51, 52]. In this approach, in the first step, the full partition function will be expanded as a series of Feynman diagrams, then employ Wick's theorem to group diagrams into determinants, and in the last step the Markov chain Monte Carlo will be used to add the resulting series [50].

The Hamiltonian of an extended Hubbard model on a two-dimensional square lattice is introduced below, we have divided the Hamiltonian into two parts, interacting part, H_{int} , and non-interacting part, H_0 given by [49]:

$$H = H_0 + H_{int}, \quad (2.32)$$

$$H_0 = - \sum_{ij\sigma} t_{ij} (c_i^\dagger c_j + h.c.) - \mu \sum_{i\sigma} n_{i\sigma} + \frac{K}{\beta}, \quad (2.33)$$

$$H_{int} = \frac{1}{2} \sum_{ij\sigma\sigma'} U_{ij}^{\sigma\sigma'} (n_{i\sigma} n_{j\sigma'} - \frac{n_{i\sigma} + n_{j\sigma'}}{2}) - \frac{K}{\beta}, \quad (2.34)$$

As we described the Hubbard model before we know that the parameters t, μ and $U_{ij}^{\sigma\sigma'}$ stand for, electrons hopping between lattice sites, the chemical potential, and the density-density interactions between electrons, respectively. Moreover, we restrict that electrons can only hop between nearest neighbour sites. The constant $\frac{K}{\beta}$ has been added to the Hamiltonians for simplicity in calculations in the next steps [50]. For interacting energy, we can have two different choices which we described them below [49]:

$$U_{ij}^{\sigma\sigma'} = \begin{cases} U \delta_{ij} \delta_{\sigma-\sigma'} \\ 0 \delta_{ij} \delta_{\sigma\sigma'}, \end{cases} \quad (2.35)$$

In this equation, the interacting energy would be U if $i = j$ and $\sigma = -\sigma'$, otherwise, it would be zero. We have Eq.2.35 to the Hubbard interaction, which is a repulsive interaction for two electrons on the same site $i = j$ and with opposite spins $\sigma = -\sigma'$.

The essential part of the partition function is the Hamiltonian. Therefore, when the Hamiltonian for a system is defined, it's easy to write the partition function, [50]

$$Z = Tr e^{-\beta H} = Tr e^{-\beta(H_0 + H_{int})}. \quad (2.36)$$

In the interaction representation the partition function can be written as

$$Z = Tr \left[e^{-\beta H_0} T_\tau e^{-\int_0^\beta d\tau H U(\tau)} \right], \quad (2.37)$$

In Eq. 2.37 T_τ represents time ordering. After expanding the exponential part of partition function, Eq. 2.37 will change to:

$$Z = \sum_{k=0}^{\infty} \int_0^\beta d\tau_1 \dots \int_{\tau_{k-1}} T_\tau \left[e^{-\beta H_0} e^{\tau_k H_0} (-H_{int}) \dots e^{-(\tau_2 - \tau_1) H_0} (-H_{int}) e^{-\tau_1 H_0} \right] \quad (2.38)$$

where $0 < \tau < \beta$ and τ displays imaginary time, also H_{int} is:

$$-H_{int} = \left(\frac{K}{4\beta N_c^2} \right) \sum_{ij\sigma\sigma'} \left(\frac{1}{2} \sum_{s=\pm 1} e^{\gamma_{ij}^{\sigma\sigma'} s(n_{i\sigma} - n_{j\sigma'})} \right) \quad (2.39)$$

N_c represents the number of cluster sites and $n_{i\sigma}$ only can take the values zero or one, so it shows the possible occupations of site i . In 2D Hubbard model $\gamma_{ij}^{\sigma\sigma'}$ is defined as:

$$\cosh(\gamma_{ij}^{\sigma\sigma'}) = \begin{cases} 1 + \frac{\beta N_c^2 U}{K} & i = j, \quad \sigma = -\sigma' \\ 1 & otherwise \end{cases} \quad (2.40)$$

Then we replace Eq. 2.40 in the partition function equation:

$$Z = \sum_{k=0}^{\infty} \sum_{\substack{s_l=\pm 1 \\ l=1,\dots,k}} \sum_{\substack{i_l,j_l,\sigma_l,\sigma'_l \\ l=1,\dots,k}} \int_0^{\beta} d\tau_1 \dots \int_{\tau_{k-1}}^{\beta} \left(\frac{K}{8\beta N_c^2} \right)^2 Z_k(s_l, \tau_l, i_l, j_l, \sigma_l, \sigma'_l) \quad (2.41)$$

In this equation Z_k is:

$$\begin{aligned} Z_k(s_l, \tau_l, i_l, j_l, \sigma_l, \sigma'_l) = & Tr[e^{-\beta H_0} \Pi_{l=k}^1 e^{\tau_l H_0} (e^{\gamma_{i_l j_l}^{\sigma_l \sigma'_l} s_l} - (e^{\gamma_{i_l j_l}^{\sigma_l \sigma'_l}} - 1) c_{i_l \sigma_l} c_{i_l \sigma'_l}^{\dagger}) \\ & \times ((e^{-\gamma_{i_l j_l}^{\sigma_l \sigma'_l} s_l} - (e^{-\gamma_{i_l j_l}^{\sigma_l \sigma'_l}} - 1) c_{j_l \sigma'_l} c_{j_l \sigma_l}^{\dagger}) e^{-\tau_l H_0}] \end{aligned} \quad (2.42)$$

We can write the partition function as a determinant of a $2k$ by $2k$ matrix N^{2k} as below [49, 53, 50]:

$$Z_k(s_l, \tau_l, i_l, j_l, \sigma_l, \sigma'_l) = \det[(N^{2k})_{ij\sigma\sigma'}^{-1}] \quad (2.43)$$

where

$$(N^{2k})_{ij\sigma\sigma'}^{-1} \equiv e^{V_{ij}^{\sigma\sigma'}} - G_{0\sigma\sigma'}^{ij} (e^{V_{ij}^{\sigma\sigma'}} - I) \quad (2.44)$$

and

$$e^{V_{ij}^{\sigma\sigma'}} \equiv \text{diag}^4(e^{-\gamma_{i_1 j_1}^{\sigma_1 \sigma'_1} s_1}, \dots, e^{-\gamma_{i_n j_n}^{\sigma_n \sigma'_n} s_n}) \quad (2.45)$$

In case the spin arguments are unequal the Green's functions would be zero, so our matrix can be block diagonalized into spin up and spin down parts. cosequently, the partition function can be rewritten as:

$$Z = \sum_{k=0}^{\infty} \sum_{\substack{s_l=\pm 1 \\ l=1,\dots,k}} \sum_{\substack{i_l,j_l,\sigma_l,\sigma'_l \\ l=1,\dots,k}} \int_0^{\beta} d\tau_1 \dots \int_{\tau_{k-1}}^{\beta} \left(\frac{K}{8\beta N_c^2} \right)^2 \det[(N_{\uparrow}^{(n)})^{-1}] \det[(N_{\downarrow}^{(m)})^{-1}] \quad (2.46)$$

⁴Diagonal terms of matrix.

To find the partition function we have to sample these series Quantum Monte Carlo methods. All possible configurations have to be sampled, and each configuration is a set of vertices. Each vertex can be described by the spin, sites, auxiliary spin, and imaginary time indices. After sampling partition functions we can find the interacting Green's function.

2.6 Susceptibility and Inversion of Bethe-Salpeter Equation

In this section, we explain how to calculate the generalized dynamical susceptibility. We use Refs. [10, 54, 55] as our main references. First, we need to define the one-particle and two-particle Green's function in imaginary time (τ) [54]:

$$G_{\sigma}(\tau_1, \tau_2) = \langle T_{\tau}(c_{\sigma_1}^{\dagger}(\tau_1)c_{\sigma_2}(\tau_2)) \rangle, \quad (2.47)$$

$$G_{2,\sigma_1\sigma_2\sigma_3\sigma_4}(\tau_1, \dots, \tau_4) = \langle T_{\tau}(c_{\sigma_1}^{\dagger}(\tau_1)c_{\sigma_2}(\tau_2)c_{\sigma_3}^{\dagger}(\tau_3)c_{\sigma_4}(\tau_4)) \rangle. \quad (2.48)$$

Where T is time-ordering operator, $c^{\dagger}(c)$ creates (annihilates) an electron with spin σ . We can define generalized susceptibility in imaginary time by using one-particle Green's function and two-particle Green's functions as follows:

$$\chi_{\sigma_1\sigma_2\sigma_3\sigma_4}(\tau_1, \tau_2, \tau_3, \tau_4) = G_{2,\sigma_1\sigma_2\sigma_3\sigma_4}(\tau_1, \dots, \tau_4) - G_{\sigma_1\sigma_2}(\tau_1, \tau_2)G_{\sigma_3\sigma_4}(\tau_3, \tau_4) \quad (2.49)$$

we can confine the problem to only three-time arguments τ_1, τ_2, τ_3 and consider $\tau_4 = 0$. Then the susceptibility would be:

$$\chi_{\sigma_1\sigma_2\sigma_3\sigma_4}(\tau_1, \tau_2, \tau_3) = G_{2,\sigma_1\sigma_2\sigma_3\sigma_4}(\tau_1, \tau_2, \tau_3, 0) - G_{\sigma_1\sigma_2}(\tau_1, \tau_2)G_{\sigma_3\sigma_4}(\tau_3, 0). \quad (2.50)$$

Moreover, by considering all symmetries we can define these spin combinations for susceptibility:

$$\chi_{\sigma\sigma'}(\tau_1, \tau_2, \tau_3) = \chi_{\sigma\sigma\sigma'\sigma'}(\tau_1, \tau_2, \tau_3) \quad (2.51)$$

$$\chi_{\sigma\sigma'}^-(\tau_1, \tau_2, \tau_3) = \chi_{\sigma\sigma'\sigma'\sigma}(\tau_1, \tau_2, \tau_3) \quad (2.52)$$



Figure 2.10: Particle-hole scattering. Taken from Ref [54] with permission.

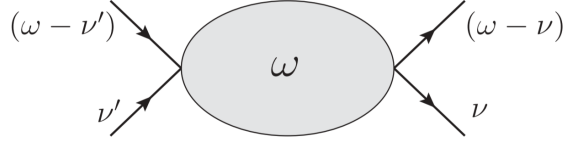


Figure 2.11: Particle-Particle scattering. Taken from Ref [54] with permission.

The susceptibility equation can be expressed in frequency space via the Fourier transform. In this space, there are two different representations, particle-hole (*ph*) and particle-particle (*pp*). Using frequency space has two main reasons. First, In the *ph* case, consider the scattering process of a hole with energy $-\nu$ and an electron with energy $\nu + \omega$, in this process the total energy is ω (this process is shown in Fig. 2.10). Second, In Fig. 2.11 the *pp* case, we look at the scattering of two electrons with energies ν and $\omega - \nu$. Again the total scattering energy will be ω . The expression for particle-hole (*ph*) and particle-particle (*pp*) susceptibilities are [54, 55]:

$$\chi_{ph\sigma\sigma'}^{\omega\omega'\Omega}(k, k', q) = \int_0^\beta d\tau_1 d\tau_2 d\tau_3 \chi_{\sigma\sigma'}(\tau_1, \tau_2, \tau_3) \times e^{-i\omega\tau_1} e^{i(\omega+\Omega)\tau_2} e^{-i(\omega'+\Omega)\tau_3} \quad (2.53)$$

where in this equation $d\tau_1 d\tau_2 d\tau_3 \chi_{\sigma\sigma'}(\tau_1, \tau_2, \tau_3)$ indicates outgoing electrons, and $e^{-i\omega\tau_1} e^{i(\omega+\Omega)\tau_2} e^{-i(\omega'+\Omega)\tau_3}$ describes incoming electrons.

$$\chi_{pp\sigma\sigma'}^{\omega\omega'\Omega}(k, k', q) = \int_0^\beta d\tau_1 d\tau_2 d\tau_3 \chi_{\sigma\sigma'}(\tau_1, \tau_2, \tau_3) \times e^{-i\omega\tau_1} e^{i(\Omega-\omega')\tau_2} e^{-i(\Omega-\omega)\tau_3} \quad (2.54)$$

In Eq.2.53 and 2.54 ω and ω' are Fermionic frequencies ($\frac{(2n+1)\pi}{\beta}$), Ω is bosonic frequency ($\frac{2m\pi}{\beta}$) and k, k', q represent momentum. We define this new notation $k = (k, \omega)$ and $q = (q, \Omega)$ for simplicity. In the interacting systems, the susceptibility can be divided into two parts, the bubble terms and vertex correction terms. Bubble term is an independent propagation of the two particles:

$$\begin{aligned} \chi_{ph\sigma\sigma'}(k, k', q) = & -\beta G_{\sigma}(k)G_{\sigma}(k+q)\delta_{kk'}\delta_{\sigma\sigma'} - G_{\sigma}(k)G_{\sigma}(k+q)F_{ph\sigma\sigma'}(k, k', q) \\ & \times G'_{\sigma}(k')G'_{\sigma}(k'+q) \end{aligned} \quad (2.55)$$

where F denotes the full vertex function which covers all accessible vertex corrections, it means, all possible scattering effects between the two propagation (the amplitude of a scattering process). The first term in right hand side of Eq. 2.55 is called bubble part, which we define it to be

$$\chi_0(k, k', q) = -\beta G_{\sigma}(k)G_{\sigma}(k+q)\delta_{kk'}\delta_{\sigma\sigma'} \quad (2.56)$$

Therefore we can rewrite Eq. 2.55 again:

$$\chi_{ph\sigma\sigma'}(k, k', q) = \chi_0(k, k', q)\delta_{\sigma\sigma'} - \frac{1}{\beta^2} \sum_{k_1 k_2} \chi_0(k, k_1, q)F_{ph\sigma\sigma'}(k_1, k_2, q)\chi_0(k_2, k', q) \quad (2.57)$$

An example calculation for the Bubble part and total susceptibility obtained from our results for $U = 5$, $\beta = 5$ and $\mu = 0$ are shown in Fig. 2.12. In these plots, we first found the Bubble part and then added it to susceptibility to find total susceptibility.

The full vertex function F includes all fully connected two-particle diagrams. These diagrams can be classified to two group, Fully irreducible and Reducible diagrams. This classification is based on the way how they can be divided by separating two internal Green's function lines.

Fully irreducible diagrams of F are those that cannot be divided into two groups, and reducible diagrams of F , can be divided by cutting two fermionic lines.

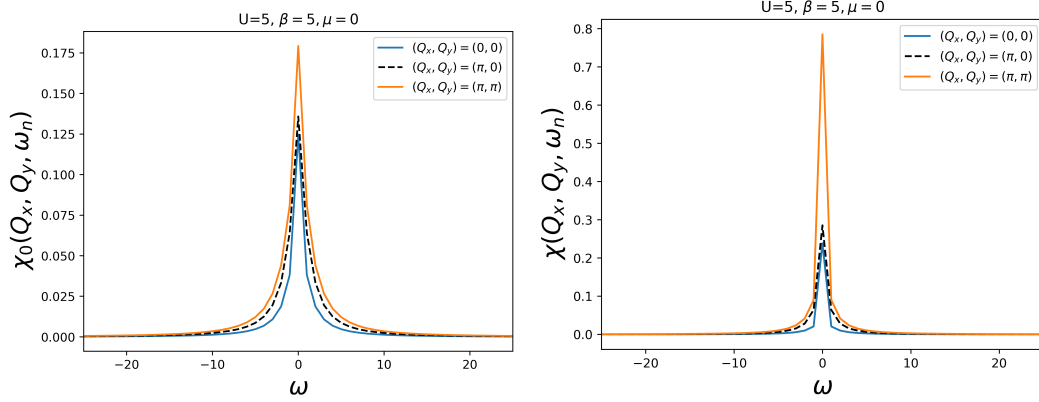


Figure 2.12: left: Bubble χ_0 vs ω (fermionic frequencies). right: χ total achieved by Eq. 2.57 vs ω (fermionic frequencies). The parameters are $U = 5$, $\beta = 5$ and $\mu = 0$.

There are different possibilities of cutting lines; therefore, the concept of reducibility has to be related to a specific channel: This defines in how two of the four outer legs of a given diagram can be divided from the other two. There are three different channels (pp, ph, \overline{ph}) , which are particle-particle, particle-hole longitudinal and transverse reducible diagrams [54].

For each of the three channels (pp, ph, \overline{ph}) there are different spin combinations and from those we are interested in two of them. They are called density (d), magnetic (m) channels given in terms of (ph) and (pp) objects as,

$$\Gamma_d = \Gamma_{ph, \uparrow\uparrow} + \Gamma_{ph, \uparrow\downarrow}, \quad (2.58)$$

$$\Gamma_m = \Gamma_{ph, \uparrow\uparrow} - \Gamma_{ph, \uparrow\downarrow}. \quad (2.59)$$

These transformations (Eqs. 2.58 and 2.59), given for Γ , also hold for χ and F functions as well. Γ and F are related to each other by Bethe-Salpeter equation:

$$F = \Gamma_r + \int \Gamma_r G G F. \quad (2.60)$$

The Bethe-Salpeter equations in the ph and ph channels are:

$$F_d(k, k', q) = \Gamma_d(k, k', q) + \frac{1}{\beta} \sum_{k_1} \Gamma_d(k, k_1, q) G(k_1) G(k_1 + q) F_d(k_1, k', q) \quad (2.61)$$

$$F_m(k, k', q) = \Gamma_m(k, k', q) + \frac{1}{\beta} \sum_{k_1} \Gamma_m(k, k_1, q) G(k_1) G(k_1 + q) F_m(k_1, k', q) \quad (2.62)$$

To find Bethe-Salpeter equations in the form of χ we need to replace above equations in Eq. 2.55. The goal is to obtain F based on χ_0 and χ , so the results are:

$$\chi_{d,m}(k, k', q) = \chi_{0,ph}(k, k', q) - \frac{1}{\beta^2} \sum_{k_1, k_2} \chi_{0,ph}(k, k_1, q) F_{d,m}(k_1, k_2, q) \chi_{0,d,m}(k_2, k', q) \quad (2.63)$$

To find two-particle full vertex function F , we use Eq. 2.63 which is in a matrix form:

$$\omega \begin{matrix} & \omega' \\ \begin{bmatrix} \chi_{\omega_1, \omega'_1, \Omega} & \cdots & \chi_{\omega_1, \omega'_N, \Omega} \\ \chi_{\omega_2, \omega'_1, \Omega} & \cdots & \chi_{\omega_2, \omega'_N, \Omega} \\ \vdots & \ddots & \vdots \\ \chi_{\omega_N, \omega'_1, \Omega} & \cdots & \chi_{\omega_N, \omega'_N, \Omega} \end{bmatrix} \end{matrix}$$

Then

$$\chi = \chi_0 - \frac{1}{\beta^2} \chi_0 F \chi_0 \quad (2.64)$$

where we can simplify it to:

$$\beta^2(\chi_0 - \chi) = \chi_0 F \chi_0 \quad (2.65)$$

The final expression for full vertex function (F) is:

$$F^{\omega, \omega', \Omega} = \beta^2(\chi_0^{-1} - \chi_0^{-1} \chi \chi_0^{-1}). \quad (2.66)$$

Where F is a two dimensional matrix. So we can use this full vertex function to build self-energy.

2.7 Dual Fermion method

The dynamical mean field theory (DMFT) provides numerically simulated results for understanding the physics of complex correlated electron systems. As we discussed before, if correlations and interactions are considered to be local, then the system can be mapped to an Anderson impurity model, which can solve it numerically [46, 56].

The dynamical mean-field approximation for local correlations is often a good approximation which can describe the general behaviour of strongly correlated material. However, DMFT is not able to explain materials where non-local correlations are important. Moreover, several fascinating phenomena in strongly correlated systems show strong momentum dependence so it is better to describe the correlations in momentum space [11, 57]. The output of DMFT solver has no momentum dependence \vec{K} [58, 59]. This problem can be solved by increasing the size of the impurity cluster to a N_c site cluster which would have N_c points in the BZ. But another problem would raise and it's that the computational cost increases [60].

Therefore a new method that can solve these problems was needed. So, the dual fermion method was introduced [11, 61, 62, 63, 64]. The method perturbatively adds corrections based from a DMFT starting point, as a result produces momentum dependent correlations. Consequently, If all corrections are added, the method retrieves the full momentum dependence of the original problem and becomes an exact solution [60].

This procedure has some advantages which make it brilliant. First, it has this ability to produce high-resolution momentum dependent quantities; moreover, this procedure has a relatively low computational cost since the number of impurity cluster is one [61, 62, 63]. We try to explain the Dual Fermions concept, and its formalism will be derived [11, 61, 62, 63, 64]. Then the Dual Fermions Ladder Approximation (DFLA), will be discussed [60, 65].

We start our discussion from the two dimensional Hubbard model with the corresponding imaginary-time action [66, 67, 68]:

$$S[c, c^*] = \sum_{\omega k \sigma} (\epsilon_k - \mu - i\omega) c_{\omega k \sigma}^* c_{\omega k \sigma} + U \sum_i \int_0^\beta n_{i\uparrow\tau} n_{i\downarrow\tau} d\tau \quad (2.67)$$

In Eq. 2.67 β represents inverse temperature ($\beta = \frac{1}{T}$) and μ is chemical potential,

$\omega_j = \frac{(2j+1)\pi}{\beta}$ where $j = 0, \pm 1, \pm 2, \dots$, and $i\omega_j$ is Matsubara frequency, the imaginary time is shown by τ , $\sigma = \uparrow, \downarrow$ describes the spin projection. The single particle dispersion on a square lattice is $\epsilon_k = -2t(\cos k_x + \cos k_y)$ and c^*, c are Grassmann variables.

We represent a single-site impurity system that is coupled to a bath by a hybridization function, Δ_ω . The action for this impurity is:

$$S_{imp} = \sum_{\omega, \sigma} (\Delta_\omega - \mu - i\omega) c_{\omega\sigma}^* c_{\omega\sigma} + U \int_0^\beta n_{\uparrow\tau} n_{\downarrow\tau} d\tau \quad (2.68)$$

The hybridization Δ is independent of k , so Eq. 2.67 (the lattice action) can be rewritten as follow:

$$S[c, c^*] = \sum_i S_{imp}[c_i, c_i^*] - \sum_{\omega k \sigma} (\Delta_\omega - \epsilon_k) c_{\omega k \sigma}^* c_{\omega k \sigma} \quad (2.69)$$

We employ a dual transformation (Hubbard-Stratonovich transformation) to introduce new Grassmann variables f, f^* :

$$e^{A^2 c_{\omega k \sigma}^* c_{\omega k \sigma}} = \left(\frac{A}{\alpha}\right)^2 \int e^{-\alpha(c_{\omega k \sigma}^* f_{\omega k \sigma} + f_{\omega k \sigma}^* c_{\omega k \sigma}) - \alpha^2 A^{-2} f_{\omega k \sigma}^* f_{\omega k \sigma}} df_{\omega k \sigma}^* df_{\omega k \sigma} \quad (2.70)$$

This identity equation is reliable for any complex numbers A and α . We can define A as $A^2 = (\Delta_\omega - \epsilon_k)$; moreover, by this assumption that $\alpha = \alpha_{\omega, \sigma}$ is momentum independent, the partition function in terms of a transformed action can be written as:

$$\begin{aligned} Z &= \int e^{-S[c, c^*]} \mathcal{D}c^* \mathcal{D}c \\ &= \int \int e^{-S[c, c^*, f, f^*]} \mathcal{D}f^* \mathcal{D}f \mathcal{D}c^* \mathcal{D}c \end{aligned} \quad (2.71)$$

that

$$\begin{aligned}
S[c, c^*, f, f^*] = & - \sum_{\omega k} \ln(\alpha_{\omega\sigma}^2(\Delta_\omega - \epsilon_k)) + \sum_i S_{imp}[c_i, c_i^*] \\
& + \sum_{\omega k\sigma} [\alpha_{\omega\sigma}(c_{\omega k\sigma}^* f_{\omega k\sigma} + f_{\omega k\sigma}^* c_{\omega k\sigma})] + \alpha_{\omega\sigma}^2(\Delta_\omega - \epsilon_k)^{-1} f_{\omega k\sigma}^* f_{\omega k\sigma}
\end{aligned} \tag{2.72}$$

Then we need to organize the relation between the Green's function of the initial system and Green's function of the dual system:

$$G_{\omega,k} = (\Delta_\omega - \epsilon_k)^{-1} \alpha_{\omega\sigma} G_{\omega,k}^{dual} \alpha_{\omega\sigma} (\Delta_\omega - \epsilon_k)^{-1} + (\Delta_\omega - \epsilon_k)^{-1} \tag{2.73}$$

Before we assumed that $\alpha_{\omega\sigma}$ is momentum independent and

$$\sum_k (f_k^* c_k + c_k^* f_k) = \sum_i (f_i^* c_i + c_i^* f_i) \tag{2.74}$$

Now we are in a position that we can integrate the action equation for each site separately. Which leads us to:

$$S_{site}[c_i, c_i^*, f_i, f_i^*] = S_{imp}[c_i, c_i^*] + \sum_\omega \alpha_{\omega\sigma} (f_\omega^* c_\omega + c_\omega^* f_\omega) \tag{2.75}$$

We can write the final action S which only depends on the new variables f, f^* :

$$S[f, f^*] = - \sum_{\omega k} \ln(\alpha_{\omega\sigma}^2(\Delta_\omega - \epsilon_k)) - \sum_i \ln z_i^{imp} + \sum_{\omega k\sigma} \alpha_{\omega\sigma} ((\Delta_\omega - \epsilon_k)^{-1} + g_\omega) \alpha_{\omega\sigma} f_{\omega k\sigma}^* f_{\omega k\sigma} + \sum_i V_i \tag{2.76}$$

In Eq. 2.76 z_i^{imp} is:

$$z_i^{imp} = \int e^{-S_{imp}[c_i, c_i^*, f_i, f_i^*]} \mathcal{D}c_i^* \mathcal{D}c_i \tag{2.77}$$

So that the partition function is

$$\int e^{-S_{site}[c_i, c_i^*, f_i, f_i^*]} \mathcal{D}c_i^* \mathcal{D}c_i = z_i^{imp} e^{\sum_{\omega\sigma} \alpha_{\omega\sigma}^2 g_\omega f_{\omega i\sigma}^* f_{\omega i\sigma} - V[f_i, f_i^*]} \tag{2.78}$$

The dual potential (V_i) includes the impurity correlation functions at all orders, and for most purposes, the dual potential can be express as [67]:

$$V \equiv V[f^*, f] = -\frac{1}{4}\gamma_{1234}^{(4)}f_1^*f_2f_3^*f_4 \quad (2.79)$$

In this approximation $\gamma^{(4)}$ is basically the 4-leg vertex function F of the local quantum impurity problem, which we defined it previously in Eq. 2.66.

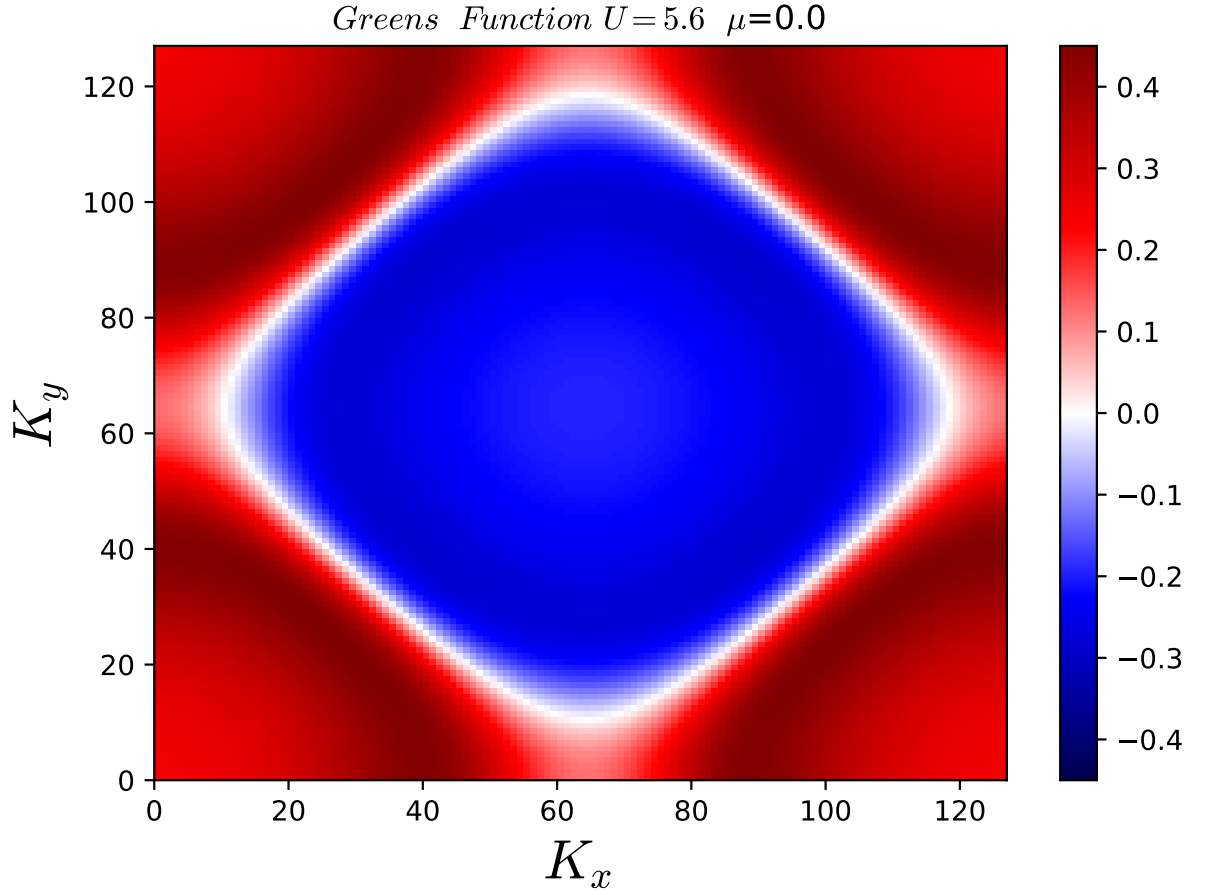


Figure 2.13: Color plot of Green's Function, Kpts resolution = 128, output of Open-DF code. In this plot we used $U = 5.6$, $\mu = 0$ and $\beta = 5$

By employing all of these changes, the total action will be:

$$S[f^*, f] = -\sum_{\omega k \sigma} f_{\omega k \sigma}^* [G_{\omega}^0(k)]^{-1} f_{\omega k \sigma} + \sum_i V_i[f_i^*, f_i]. \quad (2.80)$$

where $G_\omega^0(k)$ is bare dual Green's function and related to g_ω via:

$$G_\omega^0(k) = -g_\omega [g_\omega + (\Delta_\omega - \epsilon_k)^{-1}]^{-1} g_\omega. \quad (2.81)$$

Clearly, we changed our single particle Green's function to Dual Fermion Green's function. This Green's function now is momentum dependent and it can be expressed as $G(K_x, \omega, K_y, \omega')$. In Fig. 2.13 we showed a high resolution color plot of Green's function. The resolution in this plot is $128 * 128$, number of K points which this resolution is not accessible by using cluster DMFT methods.

2.8 Maximum Entropy Method (Maxent)

When we run dynamical mean-field solver, the output is a Green's function that is computed in imaginary time (or the Fourier transform, Matsubara frequency). However, we need to interpret it as a response function or spectral functions, which in the experiments they are measured on the real axis.

There is a big problem during direct transformations in a way that a small fluctuations of the input data (from statistical Monte Carlo noise or a truncation of the accuracy to finite precision numbers) cause large fluctuations of the output data. Several alternatives have been proposed, which among them the standard method is Maximum Entropy Method (MEM), which we will describe it in this section [69, 70, 71, 72].

The outputs of DMFT calculation is the Matsubara frequency Green's function, $G(i\omega_n)$, where:

$$i\omega_n = \begin{cases} 2\pi(n + \frac{1}{2})/\beta & \text{Fermions} \\ 2\pi n/\beta & \text{Bosons} \end{cases} \quad (2.82)$$

For fermions, the imaginary time and imaginary frequency data can be related to the real frequency Green's functions as below [69]:

$$G(i\omega_n) = \frac{-1}{\pi} \int_{-\infty}^{\infty} \frac{d\omega \operatorname{Im}[G(\omega)]}{i\omega_n - \omega} \quad (2.83)$$

$$G(\tau_n) = \frac{1}{\pi} \int_{-\infty}^{\infty} \frac{d\omega \operatorname{Im}[G(\omega)] e^{-\tau_n \omega}}{1 + e^{-\beta \omega}} \quad (2.84)$$

$\operatorname{Im}[G(\omega)]$ in the Eqs. 2.83 and 2.84 is the imaginary part of the the real frequency Green's function, that can determine the spectral function:

$$A(\omega) = -\frac{1}{\pi} \operatorname{Im}[G(\omega)] \quad (2.85)$$

Eq. 2.84 can be written in a more general form as below:

$$G_n = G(\tau_n) = \int_{-\infty}^{\infty} d\omega A(\omega) K_n(\omega) \quad (2.86)$$

$K_n(\omega)$ is the 'kernel' of the analytic continuation and is defined as:

$$K_n(\omega) = K(\tau_n, \omega) = -\frac{e^{-\tau_n \omega}}{1 + e^{-\beta \omega}} \quad (2.87)$$

This Kernel for the transformation of a fermionic Green's function from imaginary time to real frequencies axis. Kernels for Bosonic distribution functions and imaginary axis representations are as below:

$$K_n(\omega) = \frac{1}{2} \omega \frac{[e^{-\omega \tau} + e^{-\omega(\beta - \tau)}]}{1 - e^{-\beta \omega}} \quad (2.88)$$

In Fig. 2.14 we have shown Green's function in Matsubara frequency (left-hand side) which is the output of Dynamical mean-field solver, then by using open source Maxent code [69] we transformed it to the real frequency.

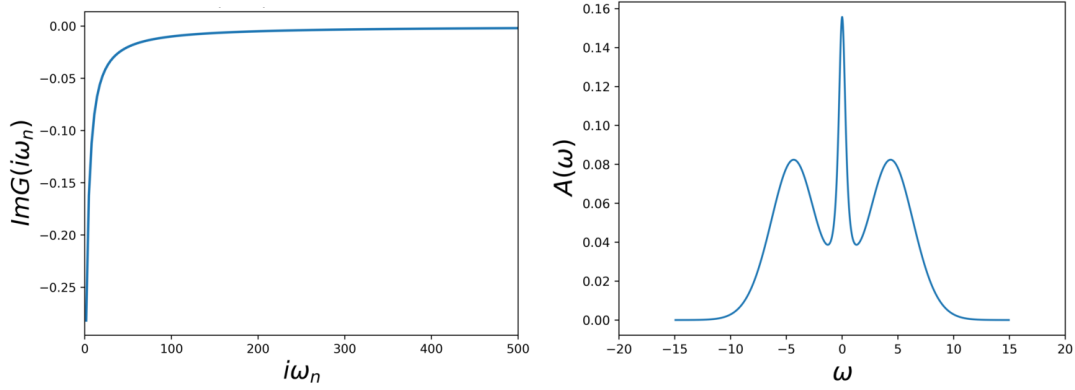


Figure 2.14: Green's function in Matsubara frequency (left) and real frequency (right), using open source Maxent code.

2.9 Fluctuation Diagnostics

Dyson- Schwinger equation of motion (EOM), link self-energy (Σ) and Vertex function (F) together. We know that the self-energy describes all scattering effects of an electron while it moves through the system. So, to define self-energy, we use two-particle scattering amplitude [73], given by

$$\Sigma(k) = \frac{U}{\beta^2 N} \sum_{k',q} F_{\uparrow\downarrow}(k, k', q) G(k') G(k' + q) G(k + q). \quad (2.89)$$

In this equation U is the Hubbard interaction, n describes density, G is electron Green's function, $\beta = \frac{1}{T}$ and N is normalization factor. F is full vertex function obtained from Eq. 2.66. So, the vertex function includes the whole information about the correlations of the two-particle system. For a better understanding of the physical role played by the scattering or fluctuation processes, we need to decompose the full scattering amplitude $F_{\uparrow\downarrow}$ of Eq. (2.89) to all possible fluctuation channels via basis transformations.

The vertex function can be expressed in different channels of spin ($F_{sp} = F_{\uparrow\uparrow} - F_{\uparrow\downarrow}$), charge or density ($F_{ch} = F_{\uparrow\uparrow} + F_{\uparrow\downarrow}$). By replacing these new vertex functions in Eq. 2.89 we can rewrite it and we can find an unique equation for each channel as follow:

$$\Sigma(k) = \frac{U}{\beta^2 N} \sum_{k',q} F_{sp}(k, k', q) G(k') G(k' + q) G(k + q), \quad (2.90)$$

$$\Sigma(k) = \frac{U}{\beta^2 N} \sum_{k', q} F_{ch}(k, k', q) G(k') G(k' + q) G(k + q). \quad (2.91)$$

If the system shows large fluctuations in any channel, it will appear in self-energy. In fact, left-hand side of Eqs. 2.90 and 2.91 are equal which represent the self-energy, but the partial sums of right-hand side of these equations are not equal. Therefore, it would let us decompose the physics in different channels. In this work we investigate the spin fluctuation, because past work has suggested that for the single band model the charge and particle-particle channels are less structured [73]. We will show some of its results in the next chapter.

2.10 Computational Methods

The first step is to find the self-energy and the Green's function of the impurity. To find these objects, we need to run the DMFT impurity solver, which we talked about it before. Therefore, the CT-AUX code, which is mpi-parallelized, will be run on the Compute Canada cluster. The iteration that we set for this code to find the self-energy and Green's function is "17". In this step, data are momentum independent. In the next step, we will run an invertor code to find the vertex function. This code works based on the Inversion of Bethe-Salpeter Equation that we mentioned before. In the last step, we access to Green's function, vertex function and self-energy then we run the open Dual Fermion (DF) code which runs on one CPU. The output of this code will be saved on a hdf5 file, the DF code gets the self energy and green's functions and susceptibility. We compute the density from the green's function. The data in this step are momentum dependent. Then data is manipulated by using python scripts to extract and analyze data for each object.

In DCA method an infinite lattice problem reduces to a finite-sized cluster impurity (instead of a single impurity as in the DMFT). So, the time of calculation will increase by " $N^3 \beta^3 U^3$ ". Where " N " is number of sites, β is chemical potential and U represents the interaction energy. DF method is linear with the number of points, or scales as " N ", but DCA is scaled as " N^3 ", which is a big difference. In this thesis we tried to solve a 64×64 problem where the number of grids is " $N = 4096$ " by open DF method, while if we want to solve this problem with DCA method it takes $4096^3 = 69$ billion times longer to solve.

Chapter 3

Results

In this section, we will present our calculations performed for the 2D Hubbard model based on DMFT and Dual Fermion calculations. We will discuss some results of densities, Green's functions, self-energy, susceptibility, correlation length and transition from Fermi liquid state to non-Fermi liquid state. As we mentioned before, to solve a strongly correlated system one of the best methods is the Dynamical Mean Field Theory. In this method, we use the continuous-time auxiliary-field algorithm (CT-AUX) as an impurity solver. The results of DMFT are the input to Dual fermion approach.

3.1 Density of states

In Fig. 3.1 we represent the density, n , versus chemical potential, μ , the slope of which is the compressibility $\kappa = \frac{\partial n}{\partial \mu}$. These plots found by DMFT methods, for different interaction strengths ($U = 3, 5, 8$). The left plot is for $\beta = 2$ and the right plot is for $\beta = 5$, also the next-nearest neighbour hopping parameter is ($t' = 0$). In these curves the density is:

$$n = \langle n_{\uparrow} + n_{\downarrow} \rangle \quad (3.1)$$

Where (\uparrow, \downarrow) describe the spin. It can be seen that by increasing β (decreasing temperature), the slope of curves increases. On the other hand, by decreasing β the slope of curves near half-filling point increases. This slope decreasing in the density vs μ plot shows its effect in the spectral function, where a gap starts to appear and represents a transition between metal and insulator. The reason for this transition

from metal to insulator is that there is no state that electron can exist in that state; therefore, the system would be an insulator. Moreover, increasing the interaction strengths around half-filling has the same result. These results are depicted in Fig. 3.3

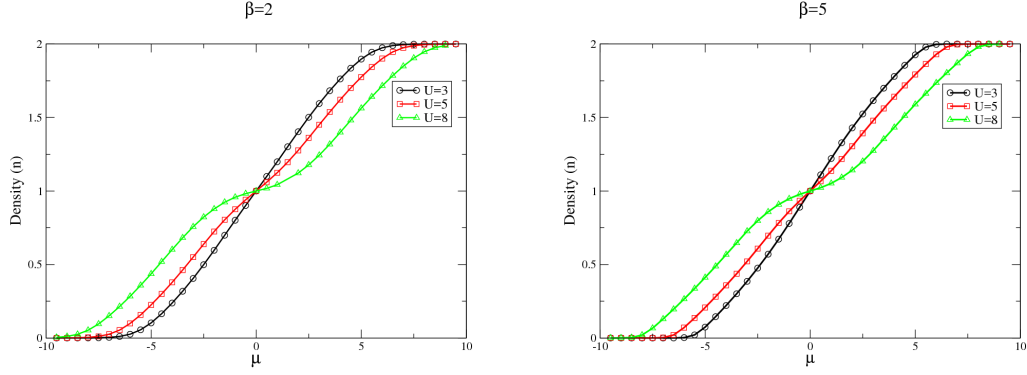


Figure 3.1: Density vs μ based on single site DMFT results for different interaction strength $U = 3, 5, 8$. In the left plot $\beta = 2$ and the right plot $\beta = 5$ and $t' = 0$.

Density in the DMFT method is obtained from $G(i\omega_n)$ which does not depend on momentum, but we have employed Dual Fermion method and this provides $G(i\omega_n, k)$. We now have access to momentum space by this correction and we can again find density vs chemical potential. In Fig. 3.2 it can be seen that around the half-filling the curve is flat for $U = 5.6$ and $U = 8$. In this plot we used $\beta = 5$ and $t' = -0.3$. This flattening shows a reduction in the compressibility of the system ($\kappa = \frac{\partial n}{\partial \mu}$), and this reduction represents an electronic gap, which means there would be a transition from metallic to insulating states.

The corrections from Dual Fermions become important at bigger interaction strengths around half-filling, and make the curve of n versus μ flat. The hopping t' brakes particle-hole symmetry, so that the curve is not symmetric around half-filling, μ . DF shows Insulator behaviour for lower U values that from DMFT.

The spectral function's plots are obtained by analytically continuing the Green's functions found by DMFT and dual fermions, via the Maximum Entropy method [72] which we discussed before. In chapter 2 we showed the relation between the spectral function and Green's function which is:

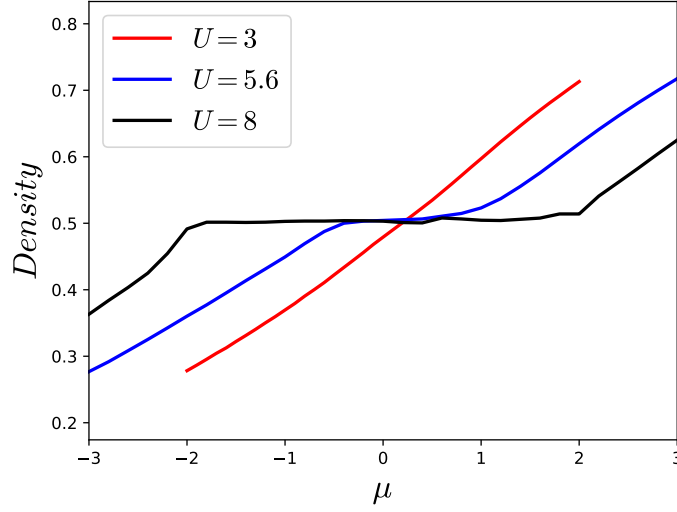


Figure 3.2: Density vs μ based on Dual Fermion approach for different interaction strength ($U = 3, 5.6, 8$) and $\beta = 5$ and $t' = -0.3$.

$$A(\omega) = -\frac{1}{\pi} \text{Im}[G(\omega)]. \quad (3.2)$$

The result of DMFT is a local Green's function which is a function of frequency, but Dual Fermion calculations produce a Green's function which has momentum as well, $G(i\omega_n, k)$, therefore to find local Dual Green's function we have to integrate over k . The density of state or local ($r = 0$) spectral function for Dual Fermion can be written as:

$$A^{DF}(\omega) = -\frac{1}{\pi} \text{Im}[\frac{1}{N_k} \sum_k G^{DF}(i\omega_n, k)], \quad (3.3)$$

where N_k is the number of momentum points. In the Fig. 3.3 the spectral function obtained from DMFT is symmetric. In the small interaction ($U = 5$) where it's called weakly correlated regime, electrons can be described as quasiparticles which their density of state still resembles free electrons. In strongly correlated regime $U = 8, 9$, the spectral function displays a three-peak structure. When the interaction between electrons are strong, $U = 12$ the metal-insulator transition occurs and force the quasiparticle peak to vanish.

In Fig. 3.4 the spectral function of Dual Fermions has been shown. As we used

$t' = -0.3$, it breaks the particle-hole symmetry of our the system, the asymmetry of the spectral functions with frequency can be seen here. Moreover, to make a comparison between Fig. 3.3 and Fig. 3.4 it can be seen that the gap of Dual Fermion at smaller U ($U = 8$) starts to open, while in DMFT the gap opens for bigger U ($U = 11$).

Dual Fermion method can produce data with any momentum space resolution that we need at lower expenses. So, Dual fermions let us to study the behaviour of Green's functions and spectral functions in the Brillouin zone. This can be advantageous for momentum dependent systems, and to make a comparison between data of simulations and data which directly come from the experimental techniques, such as ARPES [74].

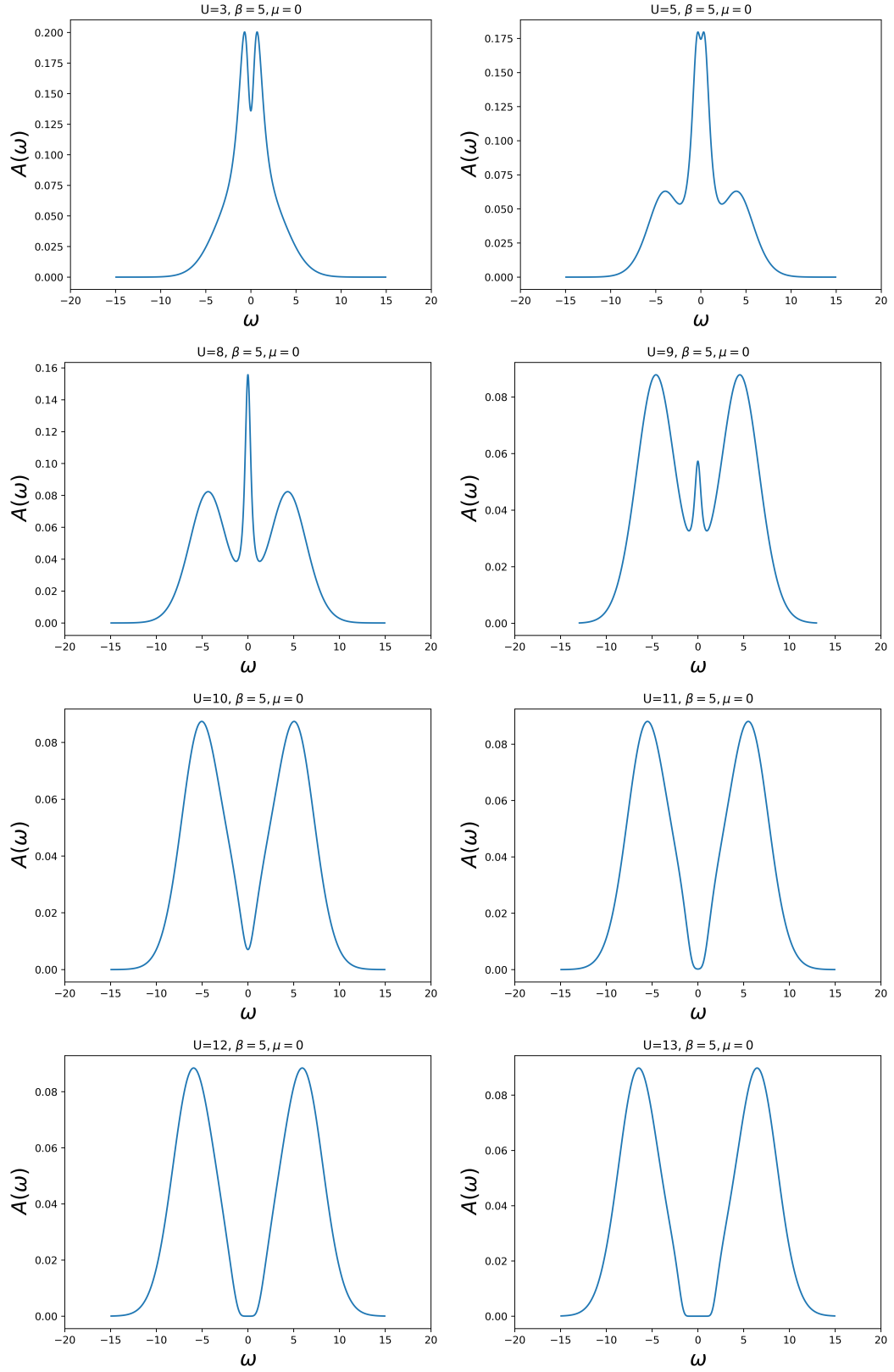


Figure 3.3: Spectral function $A(\omega)$, output of Maxent from DMFT results for $U = 3$ to $U = 13$. Transition from Fermi liquid state to non-Fermi liquid state can be seen, gap appears at $U = 12$.

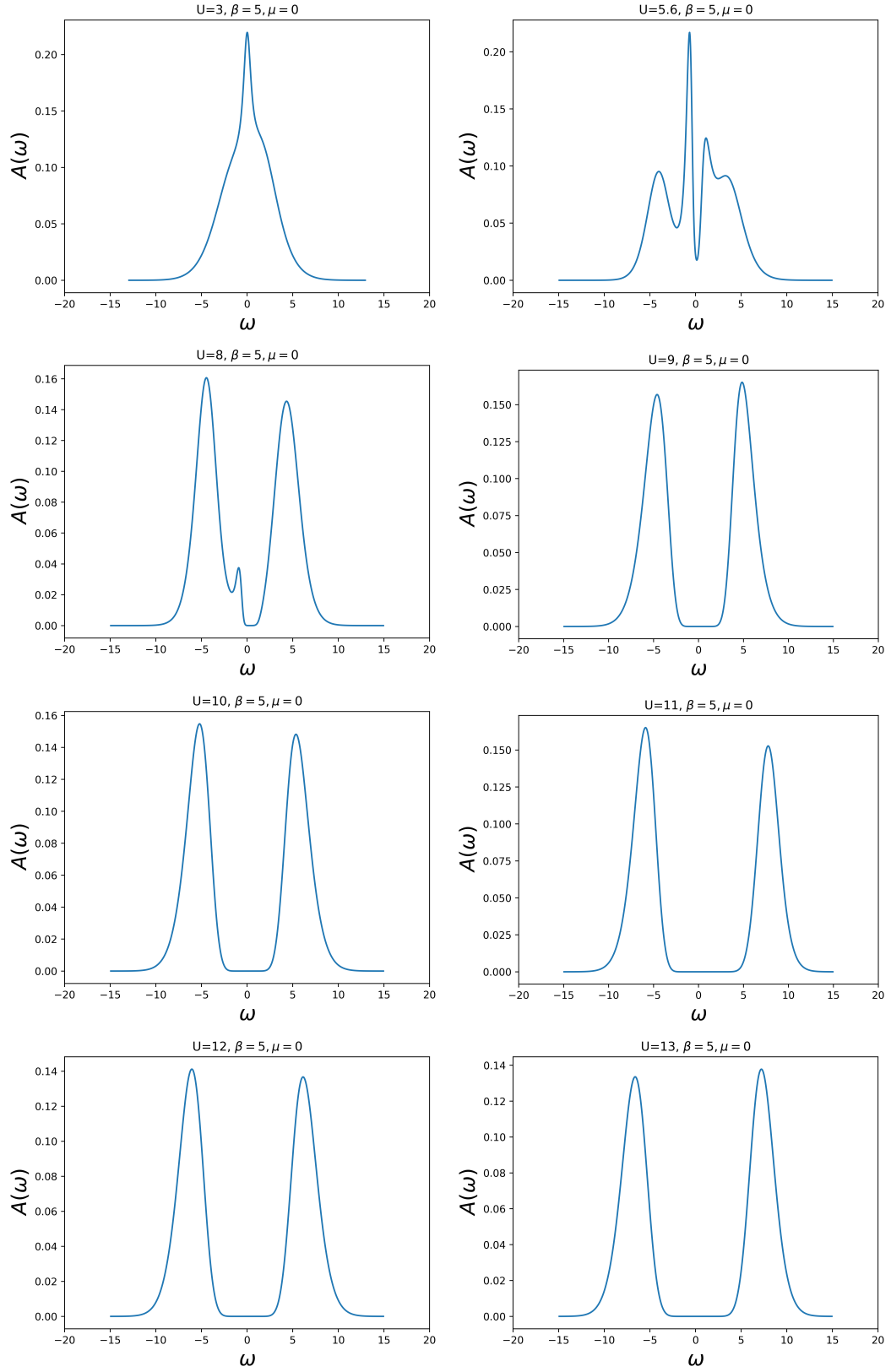


Figure 3.4: Spectral function, output of Maxent from Open- DF results for $U = 3$ to $U = 13$. Transition from Fermi liquids state to non-Fermi liquid state can be seen, gap appears between $U = 5.6$ and $U = 8$.

3.2 Dual Fermions (DF)

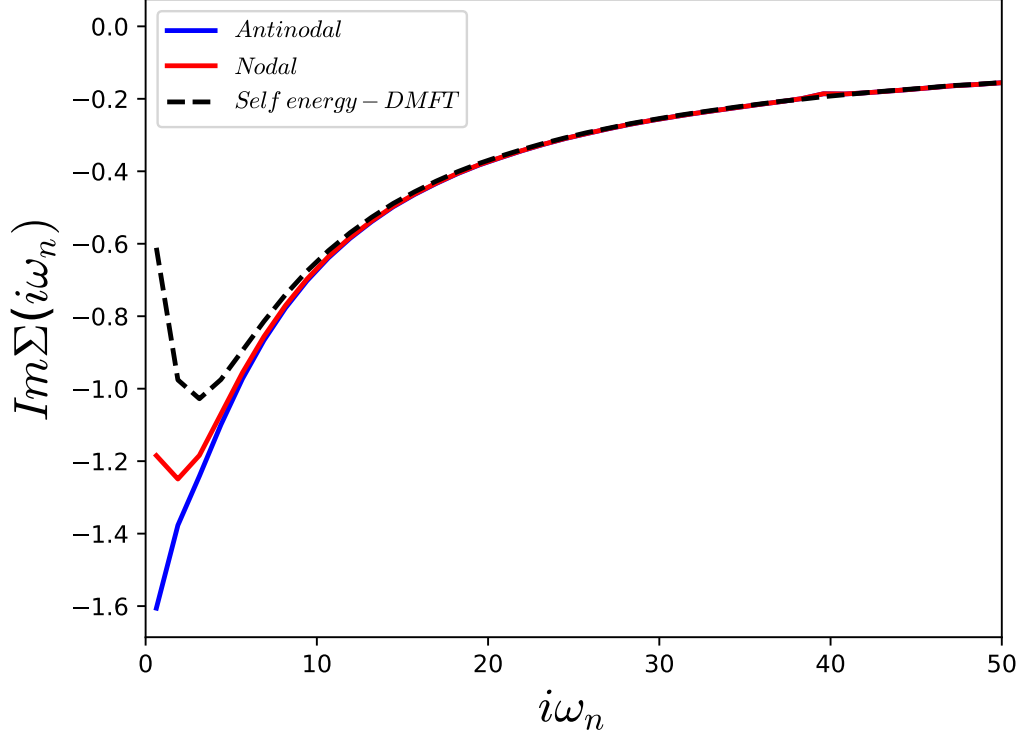


Figure 3.5: Imaginary part of the self energy as a function of Matsubara index for the DF Nodal (N) ($k = (\frac{\pi}{2}, \frac{\pi}{2})$) and Anti-nodal (AN) ($k = (0, \pi)$) results and the DMFT result. In this figure parameters for DF are $U/t = 5.6$, $\beta = 5$, $t' = -0.3$ and $\mu = 0$. Inset: Analytic continuation result for the spectral function, $A(\omega)$ for real frequency ω .

We access to DMFT self-energy ($\Sigma^{DMFT}(i\omega_n)$) and Dual Fermion self-energy ($\Sigma^{DF}(i\omega_n, k)$). For DF self-energy since we inserted momentum in our results, we can study its result in more details. So we consider two specific points in the Brillouin zone, Nodal ($k = (\frac{\pi}{2}, \frac{\pi}{2})$) and Anti-Nodal points ($k = (0, \pi)$). By comparing the two first Matsubara frequencies ($\omega_n = \frac{(2n+1)\pi}{\beta}$), we can define the status of the system ($\Delta\Sigma = \text{Im}\Sigma(i\omega_0) - \text{Im}\Sigma(i\omega_1)$). If $\text{Im}\Sigma(i\omega_0) < \text{Im}\Sigma(i\omega_1)$ ($\Delta\Sigma < 0$) the system is an insulator, otherwise, if $\text{Im}\Sigma(i\omega_0) > \text{Im}\Sigma(i\omega_1)$ ($\Delta\Sigma > 0$) the system is in Fermi Liquid regime (metallic state) [75, 76].

In Fig. 3.5 we present DF results at $U/t = 5.6$, $t' = -0.3$, $\mu = 0$, $\beta = 5$ for the imaginary part of the self energy. The DMFT result (dashed-black) shows a tendency

towards FL behaviour. It is clear that the first Matsubara frequency has a higher value than the second, so ($\Delta\Sigma > 0$). Red and blue curves are results at the nodal and antinodal momenta respectively from the DF calculation which provides momentum dependence to the self-energy. We note for these parameters the shift from FL to partial nFL behaviour indicated by the negative value of $\Delta\Sigma$ at the antinodal point and this mean the system is an insulator, while the nodal point remains with $\Delta\Sigma > 0$ and the system shows metal behaviour. This behavior is often referred to as the pseudogap phenomenon [54, 77]. Our results are in a good agreement with DiagMC and DCA calculations with similar parameters from Ref. [76].

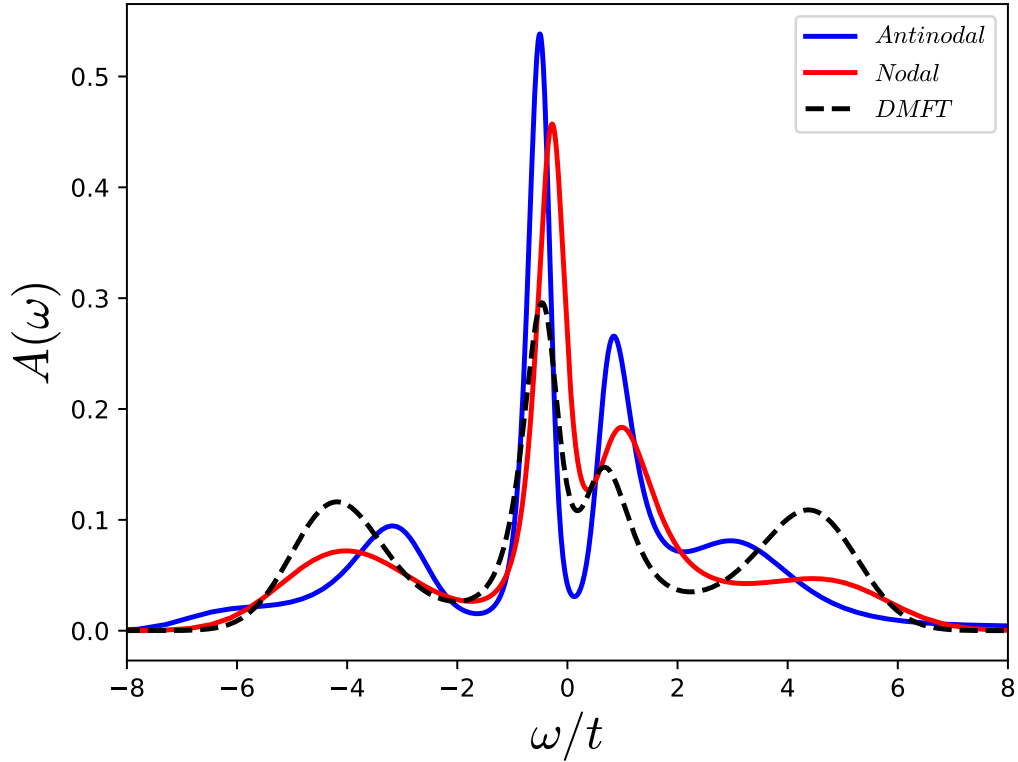


Figure 3.6: Analytic continuation result for the spectral function, $A(\omega)$ for real frequency ω . In this figure parameters for DF are $U/t = 5.6$, $\beta = 5$, $t' = -0.3$ and $\mu = 0$.

Since these results for $\beta = 5$ are at relatively high temperature, finding $\Delta\Sigma < 0$ may not be a good index of a fully gapped state. Therefore, to show this, we found their spectral function by performing analytic continuation [78] for the local-DMFT Green's function, and the Green's function for the DF nodal and antinodal results. The normalized spectral functions, $A_k(\omega)$, is shown in Fig. 3.6. Indeed, what we

have found is a non-zero density of states at the Fermi level ($\omega = 0$) that is caused by thermal excitations. We do not observe a clear $\omega = 0$ FL peak and the value of $A(\omega = 0)$ for the antinodal point is $\approx 15\%$ of the nodal value an indication of the erosion of states at the Fermi level.

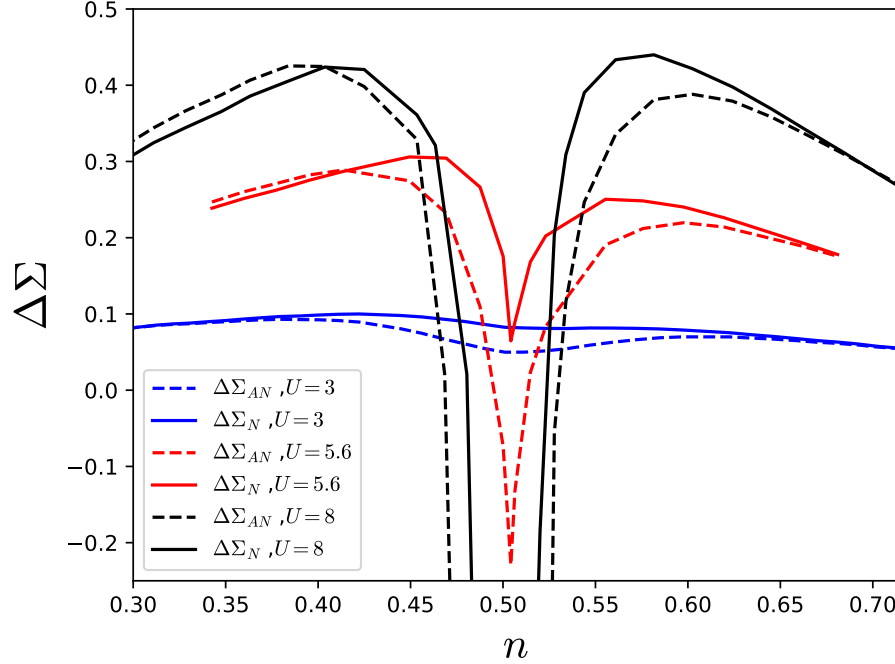


Figure 3.7: $\Delta\Sigma$ at the nodal ($\Delta\Sigma_N$) and antinodal ($\Delta\Sigma_{AN}$) momenta as a function of density for various U/t at $\beta t = 5$ and $t'/t = -0.3$.

Next, we investigate the variation of U/t and density, n , on $\Delta\Sigma$ at fixed temperature. By studying the $\Delta\Sigma$ we can reveal the behaviour of the material in different densities and show how a change in the density can change our system from FL to nFL (metallic to insulator) or vice verse.

We depict our results in Fig. 3.7 where we plot the value of $\Delta\Sigma$ at the nodal and antinodal points. At this relatively high temperature we see that at $U/t = 3$, $\Delta\Sigma$ is positive for all densities, which represent FL states at all momenta. At $U/t = 5.6$ we see a region of density near half-filling where $\Delta\Sigma_{AN} < 0$ while $\Delta\Sigma_N$ is always positive that show a mixed FL/nFL momentum separation near half-filling. For $U/t = 8$, both the nodal and antinodal points show nFL behaviour (insulator) over a range of densities (wider for the AN point) becoming positive with either electron or hole doping away from half-filling ($\mu = 0$) [79, 80]. Our results at high temperature of a

crossover with interaction strength are in agreement with the cDMFT phase diagram and shows transition from FL to nFL region [81]. What is unclear is the physical origin of the nFL behaviour, if it is a first order Mott transition or is caused by AF spin fluctuations.

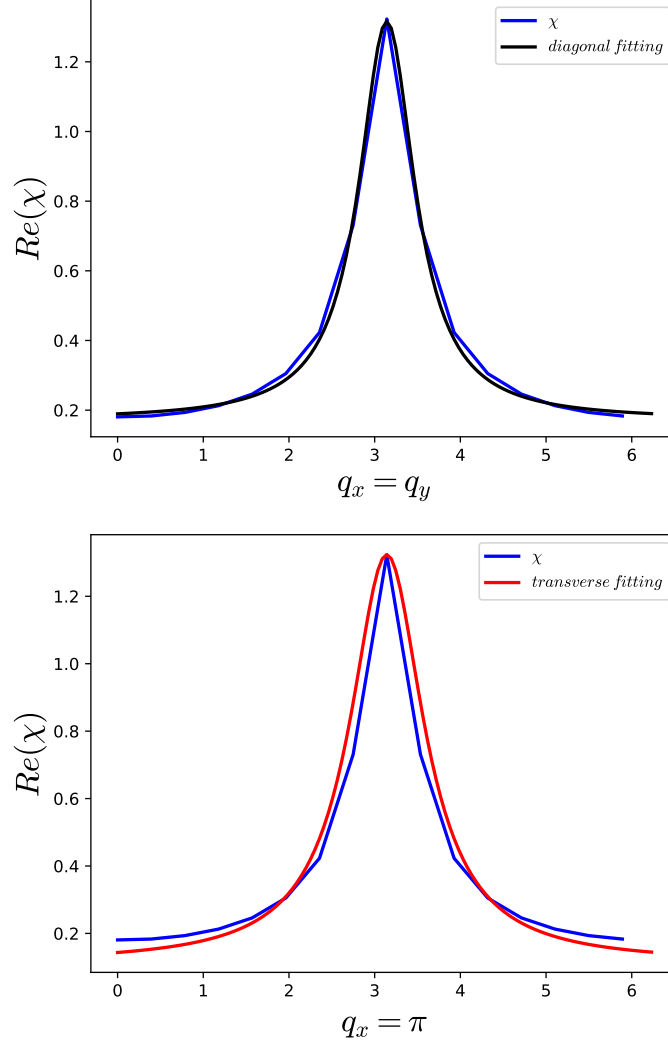


Figure 3.8: Curve fitting obtained from a fit of $\chi_{sp}(q_x, q_y, \Omega = 0)$ with the function $f(q_x, \xi) = A/((\mathbf{q} - (\pi, \pi))^2 + \xi^{-2}) + c$, averaged over the $q_x = q_y$ and $(q_x, q_y) = (q_x, \pi)$ directions, parameters are $U = 3$, $\beta = 5$ and $\mu = 0$. [82, 83]

Another output of the Dual Fermion calculations is susceptibility, $\chi_{sp}(q_x, q_y)$. χ_{sp} can be used to extract the correlation length for the system. To do this we consider the two-particle spin susceptibility [84, 85] from which we extract the correlation length. To find the correlation length we perform a curve fitting and the correlation length

would be the half-width at half-max of $\chi_{sp}(q_x, q_y, i\Omega = 0)$ near $(q_x, q_y) = (\pi, \pi)$ which can be found by fitting data to the:

$$f(q_x, \xi) = A/((\mathbf{q} - (\pi, \pi))^2 + \xi^{-2}) + c. \quad (3.4)$$

We find the half-width at half-max for two different directions $q_x = q_y$ and $(q_x, q_y) = (q_x, \pi)$ then the average of these two direction would be the correlation length Fig. 3.8 shows this process.

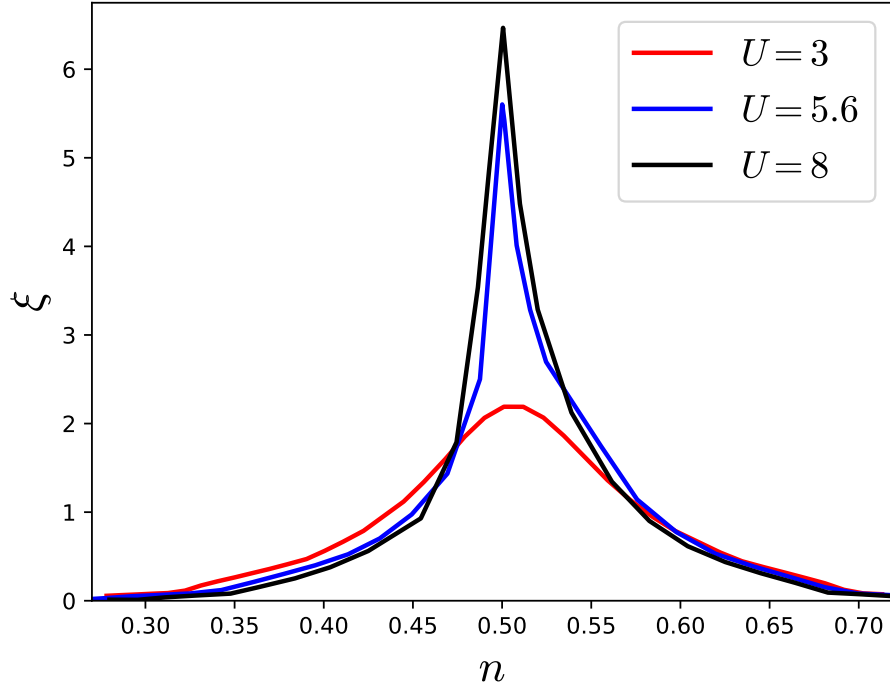


Figure 3.9: Density dependence of the anti-ferromagnetic correlation length, ξ , for several interaction strengths U at $T/t = 0.2$. Obtained from curve fitting.[82, 83]

In Fig. 3.9 we depict our results for correlation length (ξ) as a function of density for different energies. If we make a comparison between Fig. 3.7 and Fig. 3.9 we see that there is a connection between the nFL and FL behavior in the self energy as a function of density (doping) to the increase in spin-correlation length, ξ . At this high temperature for $U/t = 3$ the value of $\xi \lesssim 2$ lattice sites is quite small and comparing with Fig. 3.7 we see that $\Delta\Sigma$ is positive for all densities. At $U/t = 5.6$ and 8, ξ has a much larger value for a range of dopings near $n = 1$. It seems that the increase of ξ with doping coincides with a reduction of $\Delta\Sigma$ ultimately resulting in a change of

sign. Interestingly, at these high temperatures with modest t' , the value of $\Delta\Sigma$ is not substantially distinct between hole or electron doping ($n < 1$ and $n > 1$ respectively). The antinodal point shows a tendency towards nFL behaviour for both electron and hole doped cases. This might be because of the tendency towards antiferromagnetic behaviour that is driving the FL/nFL crossover.

3.3 Fluctuation Diagnostics

The self-energy explains all scattering effects while an electron propagates through the lattice. In correlated electronic systems, these scattering events come from the Coulomb interaction among the electrons themselves. The single particle self-energy can be determined from the full two-particle vertex function in the spin basis F_{sp} , [54, 73] and also by interacting lattice Green's function $g(k, \omega)$, which is a function of both momentum and frequency, via:

$$\Sigma(k, \omega) = \frac{Un}{2} + \frac{U}{\beta^2 N} \sum_{\bar{\omega}', \bar{\Omega}} F_{sp}^{\bar{\omega}, \bar{\omega}', \bar{\Omega}} g(\bar{\omega}') g(\bar{\omega}' + \bar{\Omega}) g(\bar{\omega} + \bar{\Omega}) \quad (3.5)$$

Where U is the Hubbard interaction, n is the density, $\beta = \frac{1}{T}$ is the inverse temperature, N is the normalization of the momentum summation, g is the electron Green's function and $\bar{\omega} = (k, \omega)$, $\bar{\omega}' = (k', \omega')$, $\bar{\Omega} = (q, \Omega)$, which ω and ω' are fermionic frequencies and Ω represents a bosonic Matsubara frequency. Choosing the basis for the full vertex has no impact on the self-energy after summation over all internal indices of the vertex [73].

In this thesis, we just study the spin channel, because former literature has suggested that for the single band model the charge and particle-particle channels are less structured, so we confined ourselves to the spin channel. Also we neglect the Hartree shift. We will study the complete set of Fermionic and Bosonic Matsubara frequencies and momentum space. To perform this we propose a partial summations given by:

$$\Sigma_k^{(x)} = \sum_{x, \bar{\omega}'} \Sigma(\bar{\omega}, \bar{\omega}', \bar{\Omega}). \quad (3.6)$$

This summation is over: positive and negative scattering momenta, $x = q$, or all bosonic frequencies, $x = +\Omega, -\Omega$ or Ω respectively; or it can be over combinations of variables such as $x = (+\Omega, q)$ which means it is a summation over positive bosonic frequencies and all q -vectors. Also, we always sum over all the internal primed fermionic elements $\bar{\omega}'$. We do this to reduce the dimensionality of our system which is convenient since $\bar{\omega}'$ does not appear in our notation, neither in either single particle self energies nor two particle susceptibilities.

In Dual Fermion method to solve two particle Green's function and vertex of the impurity problem we choose a period of fermionic and bosonic frequencies, $\Omega = -32 \rightarrow 32 = \Omega_c$ and $\omega, \omega' = -64 \rightarrow 63 = \omega_c$ inclusive. The self-energy is:

$$\Sigma(k, \omega) = \sum_{\bar{\omega}' = -\omega_c}^{\bar{\omega}' = \omega_c} \sum_{\bar{\Omega} = -\Omega_c}^{\bar{\Omega} = \Omega_c} \Sigma(\bar{\omega}, \bar{\omega}', \bar{\Omega}). \quad (3.7)$$

Fig.3.10 displays the effect of different cut off frequency on the self-energy, it proves that we have chosen the right period of Fermionic and Bosonic frequencies to remake the self-energy. The left column represents the effect of Fermionic frequencies, and the right column depicts the effect of Bosonic frequencies on the self-energy. By increasing the value of frequencies, we increase the accuracy of our solution. These plots verify that our frequency set is large enough to accurately reconstruct the DMFT and DF self energies via Eq. (3.5).

Since we can decompose the single particle $\Delta\Sigma$ into the scattering momenta (q_x, q_y) and frequency channels, we have access to different information that we are going to discuss in the following.

3.3.1 Self-energy

We start with self-energy, since we have access to all frequencies and momentum. We represent the q -vector deconstruction of self-energy in Fig. 3.11. In this figure we show the fully deconstructed self-energy contributions to the zeroth and first fermionic Matsubara frequency $i\omega_0, i\omega_1$ at $\Omega = 0$ as a function of the q -vector components. We use these two frequencies since we need to find $\Delta\Sigma$ by these two frequencies. Results of Refs [73, 76] confirm what we have found. In Fig. 3.11 we see a strong peak at $q = (\pi, \pi)$ for both the N and AN k -vectors, and weaker contributions at other

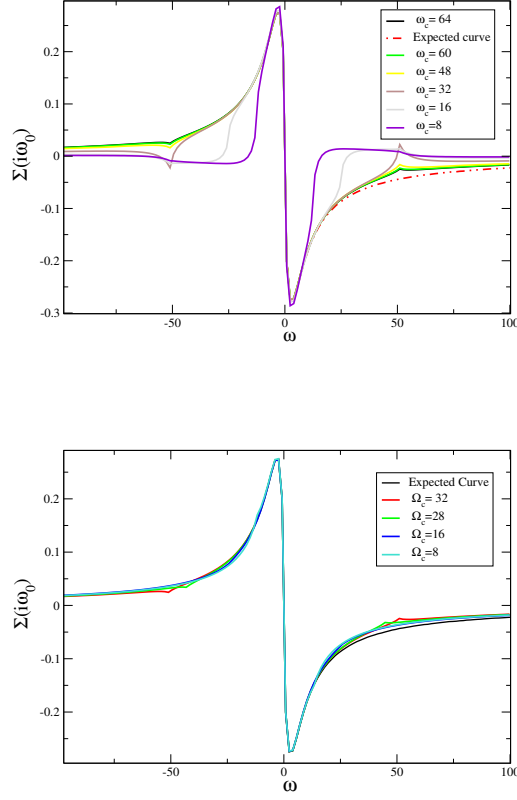


Figure 3.10: We show the effect of different cut off frequency on the self-energy. The left column represents the effect of Fermionic frequencies, and the right column depicts the effect of Bosonic frequencies on the self-energy. These plots prove that we have chosen the right period of Fermionic and Bosonic frequencies.

q -vectors. It's clear that basically all q -vector contributions to the self-energy are negative, consistent with other literature [73, 85].

In the next step, we study the effect of Bosonic frequency Ω on the self-energy. In the original fluctuation diagnostics description [73] they just studied the positive Bosonic frequencies. But to change the sign of $\Delta\Sigma$ there must also be negative contributions of Bosonic frequencies ($-\Omega$).

Therefore, we first examine the behaviour of the self energy by decomposing it into positive and negative bosonic frequency contributions. The result is depicted in Fig. 3.12. The self-energy for this case is:

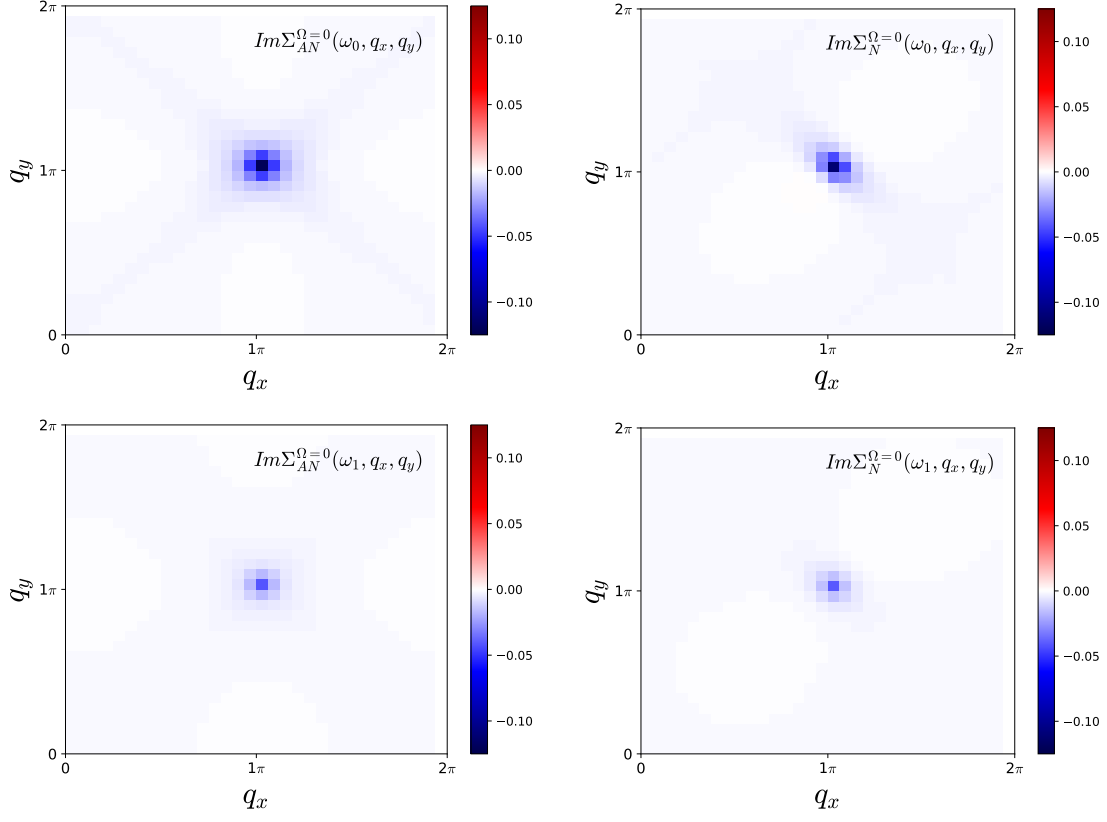


Figure 3.11: Imaginary part of the self energy for the antinodal (Left) and nodal (Right) momenta decomposed into the scattering $q = (q_x, q_y)$ contributions for the zeroth bosonic Matsubara frequency and first two Fermionic frequency for $U/t = 5.6$, $\beta t = 5$, $t'/t = -0.3$, and $\mu = 0$.

$$Im\Sigma_k^{(\Omega, q)} = Im\Sigma_k^{(+\Omega, q)} + Im\Sigma_k^{(-\Omega, q)} \quad (3.8)$$

It can be seen that to have the accurate curve of self-energy for nodal and antinodal point we have to sum over positive and negative Bosonic frequencies.

Then to see the contribution of zeroth Bosonic frequency ($\Omega = 0$) we separate this frequency. The total self energy now is this summation:

$$Im\Sigma_k(\omega) = Im\Sigma_k^{(\Omega, q)} = Im\Sigma_k^{(+\Omega, q)} + Im\Sigma_k^{(-\Omega, q)} + Im\Sigma_k^{(\Omega=0, q)} \quad (3.9)$$

Results for each component are shown in Fig. 3.13. We find that the largest contributions to the self energy come from $\Omega = 0$ which are negative for all $i\omega_n > 0$

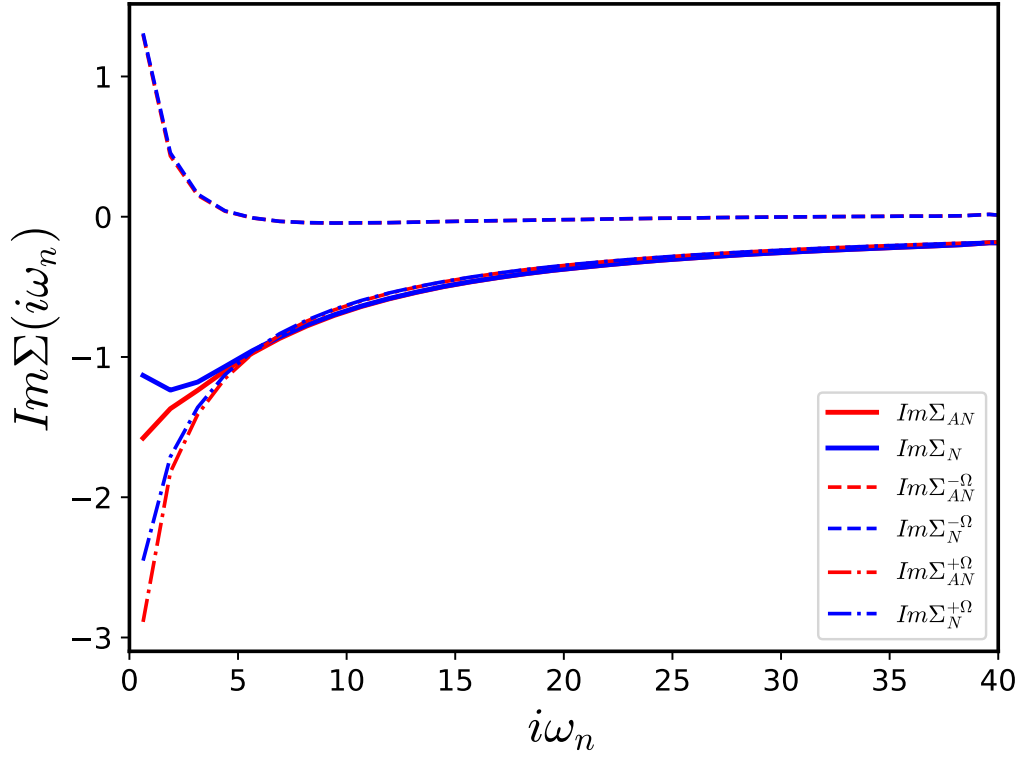


Figure 3.12: The imaginary part of the single particle self energy from Fig. 3.5 deconstructed into its $+\Omega$ and $-\Omega$ contributions at $U/t = 5.6$, $\beta t = 5$, $t'/t = -0.3$, and $\mu = 0$.

and also show a negative contribution to $\Delta\Sigma$. The summations over positive and negative bosonic frequencies decay rapidly with fermionic frequency while the $\Omega = 0$ contribution dominates the high frequency behavior. We also observe that the positive bosonic contributions are primarily negative while the negative bosonic frequency contributions are primarily positive. Interestingly, the summations over $\Omega > 0$ and $\Omega < 0$ show almost no momentum dependence. All of the momentum dependence comes from $\Omega = 0$ excitations which provide a slightly more negative contribution to $\Delta\Sigma_{AN}$ than for $\Delta\Sigma_N$. Further, the only positive contributions to $\Delta\Sigma$ come from the summation over $\Omega < 0$. Thus, deciding if $\Delta\Sigma$ is positive or negative rests on a subtle interplay between these three components. This is an element not mentioned in the original fluctuation diagnostics description [73]. These figures show that $\Delta\Sigma$ changes sign due to interplay of the $+\omega$ and $-\Omega$.

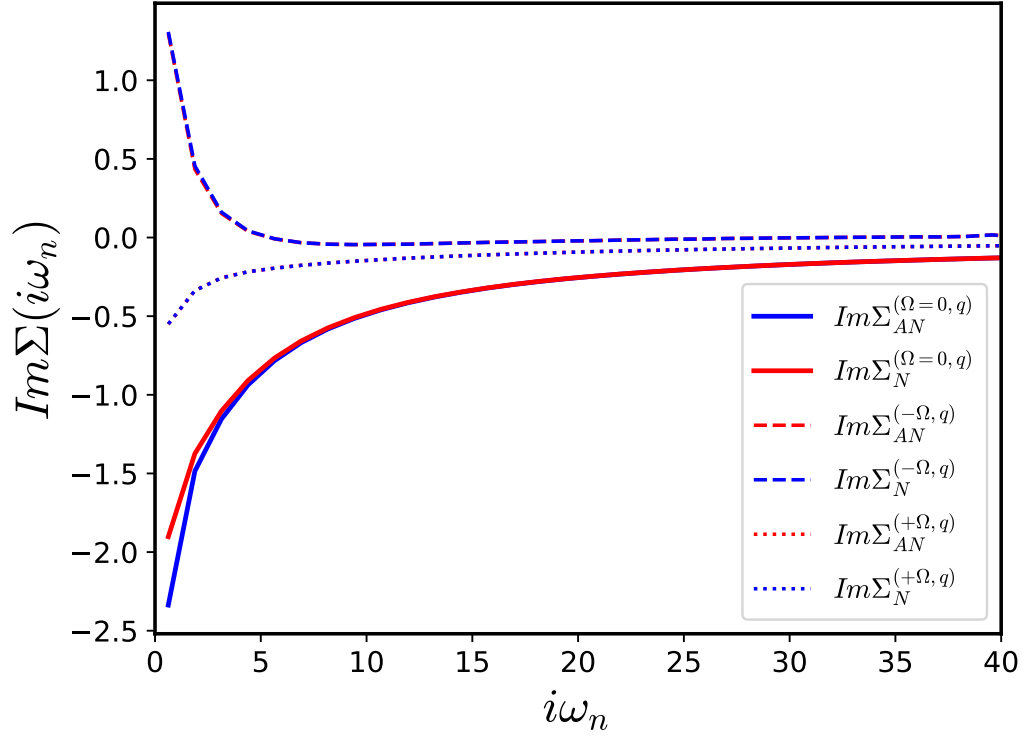


Figure 3.13: The imaginary part of the single particle self energy from Fig. 3.5 deconstructed into its $+\Omega$ and $-\Omega$ contributions and the $\Omega = 0$ contribution at $U/t = 5.6$, $\beta t = 5$, $t'/t = -0.3$, and $\mu = 0$.

Moreover, in Fig. 3.14 we show the contribution Bosonic frequencies in the self-energy of two first Fermionic frequencies. This figure reveals that the zeroth Bosonic frequency has the most contribution in the self-energy, so it's appropriate that we focus on these frequencies.

3.3.2 $\Delta\Sigma$

In Fig. 3.7 we investigated the relation between density and $\Delta\Sigma$. Now we can study doping dependency in more details. We select a range of densities for which expect $\Delta\Sigma$ to switch sign. Results for $n = 0.94, 1.0$, and 1.1 are represented in Fig. 3.15 for $\Delta\Sigma^{(\Omega)}(q_x, q_y)$ which includes the total bosonic contributions at each q_x and q_y value. This allows us to notice particularly which q -vectors give FL ($\Delta\Sigma^{(\Omega)} > 0$) contributions or nFL ($\Delta\Sigma^{(\Omega)} < 0$) contributions. We concentrate on $U/t = 5.6$ where nodal and antinodal differences happen.

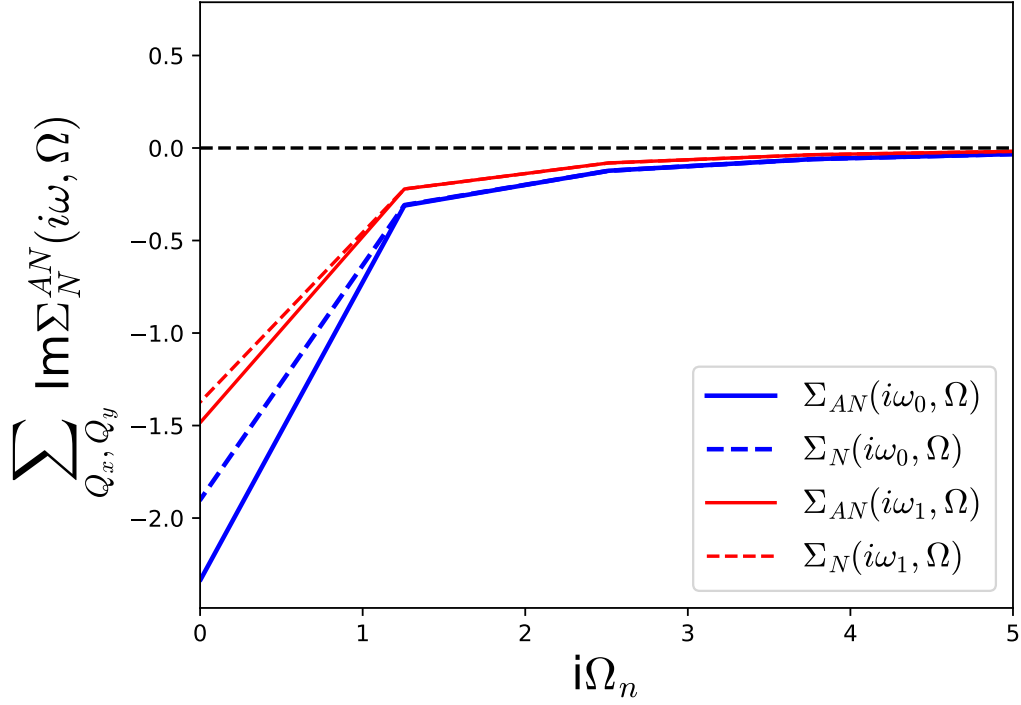


Figure 3.14: The imaginary part of the self energy deconstructed into its ω_0 and ω_1 contributions at $U/t = 5.6$, $\beta t = 5$, $t'/t = -0.3$, and $\mu = 0$. The contribution of Bosonic frequencies has been shown. It can be seen that zeroth Bosonic frequency has the most contribution in the self energy.

We see that both the antinodal and nodal frames in the top row of Fig. 3.15 (left and right columns respectively). These figures show complicated structure which include both positive and negative contributions. From Fig. 3.7 we know that the total antinodal $\Delta\Sigma_{AN} < 0$ while the total nodal $\Delta\Sigma_N > 0$ when these results are summed over q_x and q_y . For the anti-nodal frame most q -vectors provide positive contributions, which are very weak, with strong positive contributions above and below (π, π) . Also we can see there are strong negative contributions to the left and right of (π, π) . In the nodal case again most of the q -vectors give weak positive contribution and we can see both strong negative and positive peaks. In this case the strong positive feature near (π, π) overcomes the strong negative feature which finally gives an overall $\Delta\Sigma_N > 0$.

At half filling case all q -vectors give negative contributions, with the strongest feature near $q = (\pi, \pi)$. While, at $n = 1.1$ most of the q -vectors provide strong positive contributions, but the (π, π) feature remains strong and negative resulting in both the nodal and antinodal columns having a total $\Delta\Sigma > 0$ as we know is the case

from Fig. 3.7.

Finally, from the original fluctuation diagnostics work[73] we understand that the observation of the broad background for $n = 1.1$ might suggest that the spin channel is not the best (most compact) basis for describing the electron doped system.

To analyze the color plots of Fig. 3.7, plots of Fig. 3.16 includes high symmetry cuts through the Brillouin zone, which provide horizontal, vertical, and diagonal cuts through the datasets in Fig. 3.7. This plots shows cuts of $\Delta\Sigma^{(\Omega)}(q_x, q_y)$ for: (blue) for the antinodal result along the path from $(0, \pi) \rightarrow (2\pi, \pi)$, (red) is a cut for the antinodal result along the path from $(\pi, 0) \rightarrow (\pi, 2\pi)$, and (black) for the nodal result along the path from $(0, 0) \rightarrow (2\pi, 2\pi)$. The top left plot is provided for $U = 5.6$ and $\mu = -0.8$, top right plot $U = 5.6$ and $\mu = 0.0$, and the bottom plot $U = 5.6$ and $\mu = 1.4$.

In Fig.3.15 for $\mu = 0.8$ we see a complicated structure with two negative pikes left and right side of (π, π) point and two positive points below and above (π, π) point. In top-left plot of Fig.3.16 we showed exactly that for Anti-Nodal points there are two negative pikes by using a horizontal cut through the BZ ($q_y = \pi$), and vertical cut ($q_x = \pi$) reveal that there are two positive pikes above and below of (π, π) . For Nodal case, a diagonal cut ($q_x = q_y$) shows a positive pike before (π, π) and a negative pike after (π, π) .

For the half-filling case In Fig.3.15 in both Nodal and Anti-Nodal, $\Delta\Sigma = 0$ and there is a strong negative pike at the (π, π) , which we can see the same result in top right plot of Fig.3.16. Finally, for $\mu = 1.4$ in Fig. 3.15 we saw that almost $\Delta\Sigma$ for both Nodal and Anti-Nodal is positive except at (π, π) , which the bottom plot of Fig. 3.16 depicts the same result.

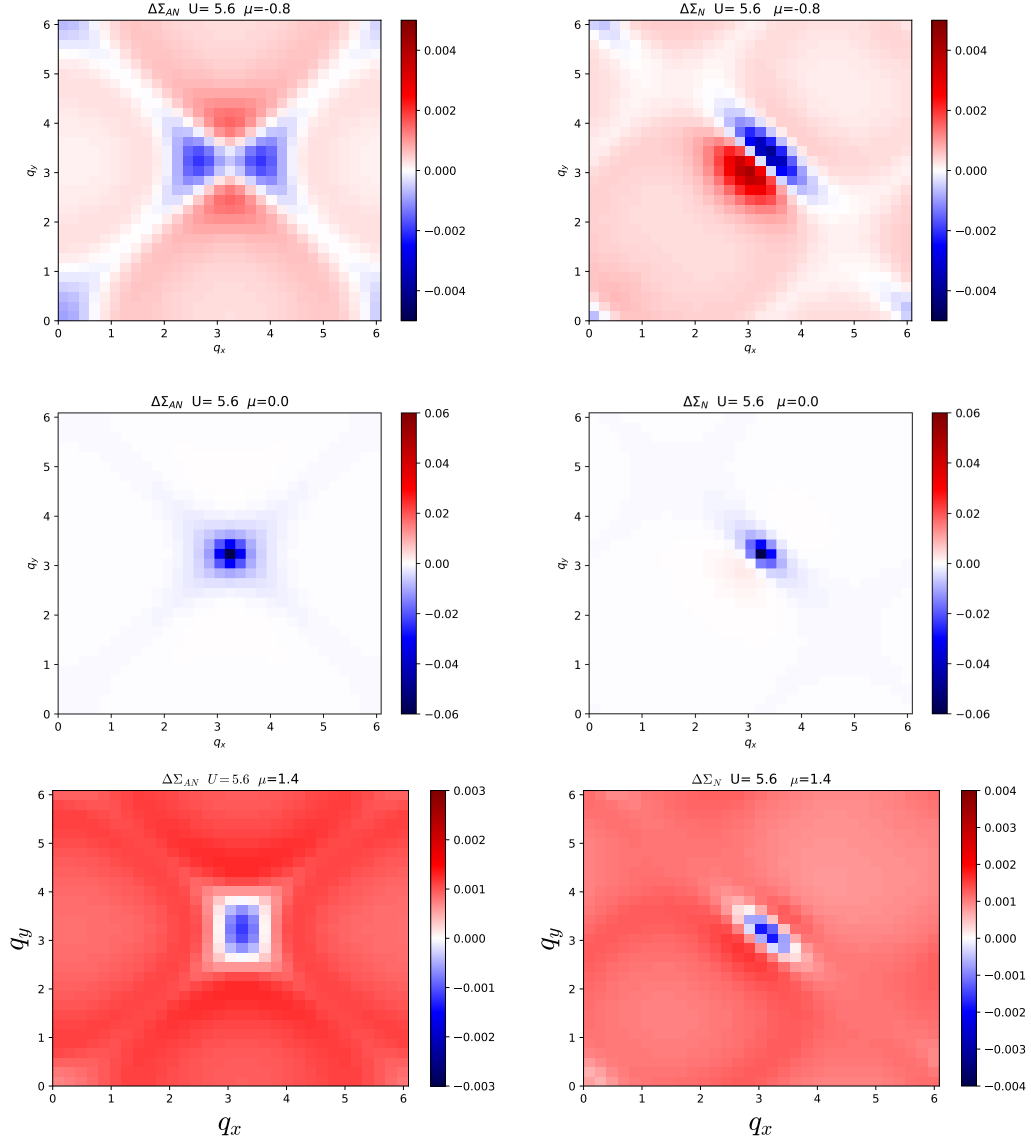


Figure 3.15: Color Plots: $\Delta\Sigma^{(\Omega)}(q_x, q_y)$ for nodal and anti-nodal momenta at $U/t = 5.6$ for $n = 0.94$ (top row), 1 (middle) and 1.1 (bottom row) corresponding to chemical potentials of $\mu/t = -0.8, 0, 1.4$ respectively.

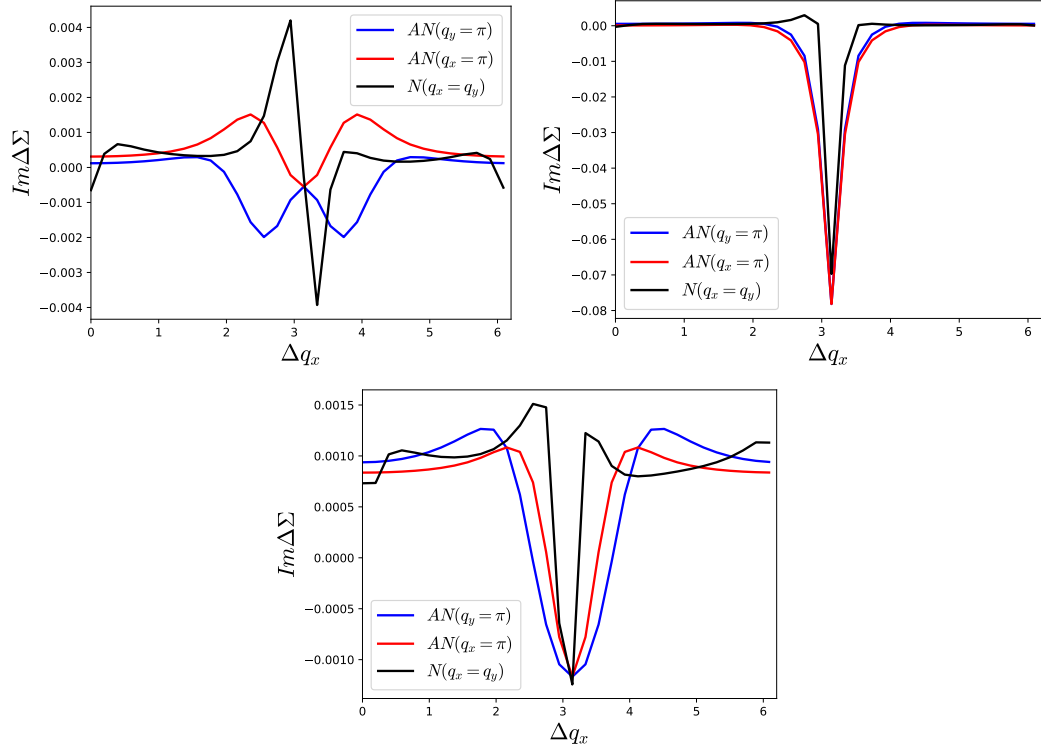


Figure 3.16: This figure shows cuts of $\Delta\Sigma^{(\Omega)}(q_x, q_y)$ for: (blue) a cut in the antinodal result along the path from $(0, \pi) \rightarrow (2\pi, \pi)$, (red) a cut in the antinodal result along the path from $(\pi, 0) \rightarrow (\pi, 2\pi)$, and (black) a cut in the nodal result along the path from $(0, 0) \rightarrow (2\pi, 2\pi)$. Each path is plotted by its length in the x-axis, normalized by the total length of the cut. The top left plot is provided for $U = 5.6$ and $\mu = -0.8$, top right plot $U = 5.6$ and $\mu = 0.0$, and the bottom plot $U = 5.6$ and $\mu = 1.4$.

Chapter 4

Conclusion

In this thesis, we studied the 2D Hubbard model using many-body theory. We used DMFT and DF methods to solve and describe the system with high momentum resolution. Calculations based on cluster extensions of dynamical mean-field theory (DCA, cDMFT), typically assume the system to be paramagnetic and suppress anti-ferromagnetic correlations during the self consistency. This is because of this assumption that in the limit of infinite cluster size the system won't have a second-order phase transition to an anti-ferromagnetic state. What was not expected is that anti-ferromagnetic spin-correlations with a finite correlation length scale could be sufficient to lead to a nFL state. It appears that small-cluster cDMFT or DCA calculations in the weak coupling regime and at low-temperatures would lead to an incorrect representation of the correlation length-scale due to a truncation of the system size. The question of precisely how these spin fluctuations cause suppression of states near the Fermi level has not been answered. To discuss this problem, we used a recent development method called fluctuation diagnostics. We used the two-particle vertex function to decompose single-particle self-energy into various basis representations and scattering channels. We represented our results in the spin channel.

In chapter 1, we presented an overview of strongly correlated phenomena, the Hubbard model and Fermi liquid theory. In chapter 2, the concept of many-body theory and numerical techniques which we used throughout the work has been provided.

Dynamical Mean Field Theory (*DMFT*), the Continuous-Time Auxiliary Field algorithm (*CT – AUX*), Dual Fermions method (*DF*) which introduce non-local correlations and provides a cheap method to obtain high resolution momentum space information, Susceptibility and vertex function F by using inverse Bethe-Salpeter Equation has been found, Fluctuation Diagnostics and the Maximum Entropy Method were all explained in this chapter.

In chapter 3, we presented our results for studying the 2D Hubbard Model on a square lattice. We described how to perform DMFT simulations on this system and use the output of DMFT as input for DF codes. We presented the result of density obtained by DMFT and Dual fermion method. Then we discussed the spectral functions which we found for both cases of DMFT and Dual Fermions results. We presented the self-energy for DMFT output as well as Nodal and Anti-nodal points obtained from Dual fermion method. We could see the transition from metal to an insulator by studying self-energy. We showed the relation between $\Delta\Sigma$ and density for different energy in Nodal and Anti-nodal region. The correlation length has been found for different energies. By Fluctuation Diagnostics method we access to any frequency we need so we showed Σ for two first frequencies. We also showed the $\Delta\Sigma$ dependence to (q_x, q_y) .

DMFT and DF helped us to find Green's function, Self-energy, and spin susceptibility function of Hubbard model on 2D square lattice. While DMFT results are momentum independent DF provides us with momentum dependent results with reasonable computational cost and high resolution momentum objects. In fact, we are able to produce high-resolution quantity in momentum space ($64 \times 64Kp$) and observe the structure of first BZ in more details, while other researchers by using DCA method only could use 8-site calculation [73]. Our results ($64 \times 64Kp = 4096$) in comparison with DCA research on 8 – sites, our system is 512 times larger, while it is faster and not as expensive as DCA method. The spectral function obtained by DF shows phase transition in smaller U in comparison with DMFT results. Moreover, we showed that zeroth Bosonic Frequency has the most contribution in the Self-energy function.

Bibliography

- [1] Gabriel Kotliar and Dieter Vollhardt. Strongly correlated materials: Insights from dynamical mean-field theory. *Physics Today*, 57:53, March 2004.
- [2] Piers Coleman. *Introduction to Many-Body Physics*. Cambridge University Press, 2015.
- [3] Vladimir Anisimov and Yuri Izyumov. *Electronic Structure of Strongly Correlated Materials*. Springer, 2010.
- [4] Elbio Dagotto. Complexity in strongly correlated electronic systems. *American Association for the Advancement of Science*, 309, 2005.
- [5] Naoto Nagaosa Patrick A. Lee and Xiao-Gang Wen. Doping a mott insulator: Physics of high-temperature superconductivity. *Reviews of Modern Physics*, 78, 2006.
- [6] Patrick A. Lee and Xiao-Gang Wen. Unusual superconducting state of underdoped cuprates. *Physical Review Letters*, 78, 1997.
- [7] J. E. Gubernatis R. T. Scalettar S. R. White D. J. Scalapino E. Y. Loh, Jr. and R. L. Sugar. Sign problem in the numerical simulation of many-electron systems. *Physical Review B*, 41, 1990.
- [8] Hao Shi and Shiwei Zhang. Infinite variance in fermion quantum monte carlo calculations. *Physical Review E*, 93, 2016.
- [9] U. Schollwock. The density-matrix renormalization group. *Reviews of Modern Physics*, 77, 2005.
- [10] Thomas Pruschke Thomas Maier, Mark Jarrell and Matthias H. Hettler. Quantum cluster theories. *Reviews of Modern Physics*, 77, 2005.
- [11] M. I. Katsnelson A. N. Rubtsov and A. I. Lichtenstein. Dual fermion approach to nonlocal correlations in the hubbard model. *Physical Review B*, 77, 2008.
- [12] Charles Kittel. *Introduction to Solid State Physics*. WILEY, 2004.

- [13] L.D. Landau and E.M. Lifshitz. *Statistical Physics*. Oxford, 1980.
- [14] Philippe Nozieres. *Theory Of Interacting Fermi Systems*. Westview Press, 1997.
- [15] G. Baym and C. Pethick. *Landau Fermi-liquid theory*. WILEY, 1991.
- [16] L D. Landau. The theory of a fermi liquid. *Soviet Physics JETP*, 3, 1956.
- [17] Mark Jarrell. *The Electronic Fermi Liquid- chapter 6*. 2017.
- [18] A. J. Schofield. Non-fermi liquids. *Contemporary Physics*, 40, 1999.
- [19] Wim van Saarloos C.M.Varma, Z.Nussinov. Singular or non-fermi liquids. *Physics Reports*, 361, 2002.
- [20] G. R. Stewart. Non-fermi-liquid behavior in d- and f-electron metals. *Reviews of Modern Physics*, 73, 2001.
- [21] H. J. Schulz. Fermi liquids and non-fermi liquids. *arXiv*, DOI:arXiv:cond-mat/9503150, 1995.
- [22] Martin C. Gutzwiller. Effect of correlation on the ferromagnetism of transition metals. *Physical Review Letters*, 10, 1963.
- [23] J. Hubbard. Electron correlations in narrow energy bands. *Royal Society*, 276, 1963.
- [24] Arianna Montorsi. *The Hubbard Model*. World Scientific, 1992.
- [25] Mario Rasetti. *The Hubbard Model Recent Results*. World Scientific, 1991.
- [26] Fabian Essler, Holger Frahm, and Frank Gohmann. *The One Dimensional Hubbard Model*. Cambridge University Press, 2005.
- [27] Richard D. Mattuck. *A Guide to Feynman Diagrams in the Many-body Problem*. Dover Publications, 1992.
- [28] Erik Koch Eva Pavarini and Ulrich Schollwöck. *Emergent Phenomena in Correlated Matter (Lecture Notes of the Autumn School Correlated Electrons)*. 2013.
- [29] Beatriz G. Prado Mariana M. Odashima and E. Vernek. Pedagogical introduction to equilibrium green's functions: condensed-matter examples with numerical implementations. *Revista Brasileira de Ensino de Física*, 39, 2017.
- [30] Eleftherios N. Economou. *Green's Functions in Quantum Physics*. Springer, 2006.
- [31] David Kaiser. *Drawing Theories Apart The Dispersion of Feynman Diagrams in Postwar Physics*. University of Chicago Press, 2005.

- [32] James Robert Brown. How do feynman diagrams work? *Perspectives on Science*, 26, 2018.
- [33] David Kaiser. Physics and feynman's diagrams. *American Scientist*, 93, 2005.
- [34] Andre-Marie Tremblay. *A refresher in many-body theory*. Sherbrooke University, May 2008.
- [35] G. C. Wick. The evaluation of the collision matrix. *Physical Review*, 80, 1950.
- [36] B. Westwanski. Thermodynamical and green function many-body wick theorems. *Physica*, 140, 1987.
- [37] Sam T Carr. *Quantum Field Theory II An introduction to Feynman diagrams*. University of Birmingham, 2009.
- [38] Thomas Strohm. *A short tutorial on Green's functions*. extracted from PhD thesis, Nov 2004.
- [39] Dimitri Van Neck Willem H Dickhoff. *Many-Body Theory Exposed! Propagator description of quantum mechanics in many-body systems*. World Scientific Publishing Co. Pte. Ltd, 2005.
- [40] Michael V. Sadovskii. *Diagrammatics Lectures on Selected Problems in Condensed Matter Theory*. World Scientific Publishing Co. Pte. Ltd, March 2006.
- [41] Dmitri Ivanov. *Condensed matter theory Lecture notes and problem sets*. 2012-2013.
- [42] P. W. Anderson. Localized magnetic states in metals. *Physical Review*, 124, 1961.
- [43] J. de Boer W.J. de Haas and G.J. van den Berg. The electrical resistance of gold, copper and lead at low temperatures. *Physica*, 1, 1934.
- [44] Carlos Gonzalez-Buxton and Kevin Ingersent. Renormalization-group study of anderson and kondo impurities in gapless fermi systems. *Physical Review B*, 57, 1998.
- [45] Alexander Cyril Hewson. *The Kondo Problem to Heavy Fermions*. Cambridge University Press, 1993.
- [46] Walter Metzner and Dieter Vollhardt. Correlated lattice fermions in $d=\infty$ dimensions. *Physical Review Letters*, 62, 1989.
- [47] Werner Krauth Antoine Georges, Gabriel Kotliar and Marcelo J. Rozenberg. Dynamical mean-field theory of strongly correlated fermion systems and the limit of infinite dimensions. *Rev. Mod. Phys*, 68, 1996.

- [48] Gerald D. Mahan. *Condensed Matter in a Nutshell*. Princeton University Press, 2011.
- [49] Tianran Chen Hanna Terletska and Emanuel Gull. Charge ordering and correlation effects in the extended hubbard model. *Physical Review B*, 95, March 2017.
- [50] O. Parcollet E. Gull¹, P. Werner and M. Troyer. Continuous-time auxiliary-field monte carlo for quantum impurity models. *Europhysics Letters Association*, 82, 2008.
- [51] Joseph E. Paki. *Quantum Monte Carlo Methods and Extensions for the 2D Hubbard Model*. A dissertation submitted in partial fulfillment of the requirements for the degree of Doctor of Philosophy (Physics) in the University of Michigan, 2019.
- [52] Sebastian Fuchs Phani Nukala Michael S. Summers Thomas Pruschke Thomas C. Schulthess Emanuel Gull, Peter Staar and Thomas Maier. Submatrix updates for the continuous-time auxiliary field algorithm. *Physical Review B*, 83, 2011.
- [53] K. Haule V. S. Oudovenko O. Parcollet G. Kotliar, S. Y. Savrasov and C. A. Marianetti. Electronic structure calculations with dynamical mean-field theory. *Reviews of Modern Physics*, 78, 2006.
- [54] A. Valli G. Rohringer and A. Toschi. Local electronic correlation at the two-particle level. *Physical Review B*, 86, 2012.
- [55] K. Mielson M. Jarrell, A. Macridin and J.E. Gubernatis D.G.S.P. Doluweera. The dynamical cluster approximation with quantum monte carlo cluster solvers. *Lectures on the Physics of Strongly Correlated Systems XII*.
- [56] E. Muller-Hartmann. Correlated fermions on a lattice in high dimensions. *Z. Phys. B - Condensed Matter*, 74, 1989.
- [57] Hartmut Hafermann Erik G. C. P. van Loon and Mikhail I. Katsnelson. Precursors of the insulating state in the square-lattice hubbard model. *Physical Review B*, 97, February 2018.
- [58] Emanuel Gull Andrey E. Antipov, James P.F. LeBlanc. Opendf - an implementation of the dual fermion method for strongly correlated systems. *Physics Procedia*, 68, 2015.
- [59] M. Jarrell M. H. Hettler, M. Mukherjee and H. R. Krishnamurthy. Dynamical cluster approximation: Nonlocal dynamics of correlated electron systems. *Physical Review B*, 61, May 2000.

- [60] Federico Becca Ireneusz W. Bulik Garnet Kin-Lic Chan Chia-Min Chung Youjin Deng Michel Ferrero Thomas M. Henderson Carlos A. Jimenez-Hoyos E. Kozik Xuan-Wen Liu Andrew J. Millis N. V. Prokof'ev Mingpu Qin Gustavo E. Scuseria Hao Shi B. V. Svistunov Luca F. Tocchio I. S. Tupitsyn Steven R. White Shiwei Zhang Bo-Xiao Zheng Zhenyue Zhu J. P. F. LeBlanc, Andrey E. Antipov and Emanuel Gull. Solutions of the two-dimensional hubbard model: Benchmarks and results from a wide range of numerical algorithms. *Physical Review X*, 5, December 2015.
- [61] T. Pruschke J. Moreno P. Haase, S.-X. Yang and M. Jarrell. Dual-fermion approach to the anderson-hubbard model. *Physical Review B*, 95, 2017.
- [62] A. N. Rubtsov M. I. Katsnelson A. I. Lichtenstein H. Hafermann, G. Li and H. Monien. Efficient perturbation theory for quantum lattice models. *Physical Review Letters*, 102, 2009.
- [63] Hartmut Hafermann Junya Otsuki and Alexander I. Lichtenstein. Superconductivity, antiferromagnetism, and phase separation in the two-dimensional hubbard model: A dual-fermion approach. *Physical Review B*, 90, 2014.
- [64] H. Terletska Z. Y. Meng T. Pruschke J. Moreno S.-X. Yang, P. Haase and M. Jarrell. Dual-fermion approach to interacting disordered fermion systems. *Physical Review B*, 89, 2014.
- [65] A. I. Lichtenstein A. N. Rubtsov, M. I. Katsnelson. Dual boson approach to collective excitations in correlated fermionic systems. *Annals of Physics*, 327, May 2012.
- [66] A. I. Lichtenstein A. N. Rubtsov, M. I. Katsnelson and A. Georges. Dual fermion approach to the two-dimensional hubbard model: Antiferromagnetic fluctuations and fermi arcs. *Physical Review B*, 79, January 2009.
- [67] A. N. Rubtsov M. I. Katsnelson A. Georges H. Hafermann, F. Lechermann and A. I. Lichtenstein. *Strong electronic correlations: Dynamical mean-field theory and beyond, in Modern Theories of Many-Particle Systems in Condensed Matter Physics*. Springer, 2012.
- [68] Alexander Lichtenstein. *Path Integrals and Dual Fermions*. Universitat Hamburg, 2017.
- [69] Emanuel Gull Ryan Levya, J.P.F. LeBlanc. Implementation of the maximum entropy method for analytic continuation. *Computer Physics Communications*, 215, 2017.
- [70] D. S. Sivia R. N. Silver and J. E. Gubernatis. Maximum-entropy method for analytic continuation of quantum monte carlo data. *Physical Review B*, 41, 1990.

- [71] Thomas Pruschke Sebastian Fuchs and Mark Jarrell. Analytic continuation of quantum monte carlo data by stochastic analytical inference. *Physical Review B*, 81, May 2010.
- [72] M. Jarrell. *Maximum Entropy Analytic Continuation Of Quantum Monte Carlo Data*. Lectures on the Physics of Strongly Correlated Systems XII, 2005.
- [73] O. Gunnarsson, T. Schäfer, J. P. F. LeBlanc, E. Gull, J. Merino, G. Sangiovanni, G. Rohringer, and A. Toschi. Fluctuation diagnostics of the electron self-energy: Origin of the pseudogap physics. *Phys. Rev. Lett.*, 114:236402, Jun 2015.
- [74] Zahid Hussain Andrea Damascelli and Zhi-Xun Shen. Angle-resolved photoemission studies of the cuprate superconductors. *Reviews of Modern Physics*, 75, 2003.
- [75] D. Rost G. Rohringer E. Arrigoni K. Held N. Blumer-M. Aichhorn T. Schafer, F. Geles and A. Toschi. Fate of the false mott-hubbard transition in two dimensions. *Physical Review B*, 91, March 2015.
- [76] Antoine Georges Wei Wu, Michel Ferrero and Evgeny Kozik. Controlling feynman diagrammatic expansions: Physical nature of the pseudogap in the two-dimensional hubbard model. *Physical Review B*, 96, 2017.
- [77] Kai-Yu Yang T M Rice and F C Zhang. A phenomenological theory of the anomalous pseudogap phase in underdoped cuprates. *Rep. Prog. Phys*, 75, 2012.
- [78] Alexander I. Lichtenstein Alexey N. Rubtsov Matthias Troyer Emanuel Gull, Andrew J. Millis and Philipp Werner. Continuous-time monte carlo methods for quantum impurity models. *Reviews of Modern Physics*, 83, 2011.
- [79] E. Gull, M. Ferrero, O. Parcollet, A. Georges, and A. J. Millis. Momentum-space anisotropy and pseudogaps: A comparative cluster dynamical mean-field analysis of the doping-driven metal-insulator transition in the two-dimensional hubbard model. *Phys. Rev. B*, 82:155101, Oct 2010.
- [80] Emanuel Gull, Olivier Parcollet, Philipp Werner, and Andrew J. Millis. Momentum-sector-selective metal-insulator transition in the eight-site dynamical mean-field approximation to the hubbard model in two dimensions. *Phys. Rev. B*, 80:245102, Dec 2009.
- [81] H. Park, K. Haule, and G. Kotliar. Cluster dynamical mean field theory of the mott transition. *Phys. Rev. Lett.*, 101:186403, Oct 2008.
- [82] G. Rohringer and A. Toschi. Impact of nonlocal correlations over different energy scales: A dynamical vertex approximation study. *Phys. Rev. B*, 94:125144, Sep 2016.

- [83] Jan Gukelberger, Evgeny Kozik, and Hartmut Hafermann. Diagrammatic monte carlo approach for diagrammatic extensions of dynamical mean-field theory: Convergence analysis of the dual fermion technique. *Phys. Rev. B*, 96:035152, Jul 2017.
- [84] S. Brener, H. Hafermann, A. N. Rubtsov, M. I. Katsnelson, and A. I. Lichtenstein. Dual fermion approach to susceptibility of correlated lattice fermions. *Phys. Rev. B*, 77:195105, May 2008.
- [85] Xi Chen, J. P. F. LeBlanc, and Emanuel Gull. Simulation of the nmr response in the pseudogap regime of the cuprates. *Nature Communications*, 8:14986, Apr 2017. Article.